

<https://doi.org/10.1038/s42003-025-08632-5>

Human neural organoid microphysiological systems show the building blocks necessary for basic learning and memory

Check for updates

Dowlette-Mary Alam El Din^{1,2}, Leah Moenkemoeller¹, Alon Loeffler³, Forough Habibollahi³, Jack Schenkman⁴, Amitav Mitra⁵, Tjitse van der Molen^{6,7}, Lixuan Ding¹, Jason Laird^{1,2}, Maren Schenke^{1,2}, Erik C. Johnson⁸, Brett J. Kagan^{3,9}, Thomas Hartung^{1,2,10,11} & Lena Smirnova^{1,2} ✉

Brain Microphysiological Systems, including neural organoids derived from human induced pluripotent stem cells, offer a unique lens to study the intricate workings of the human brain. This paper investigates the foundational elements of learning and memory in neural organoids by quantifying immediate early gene expression in response to chemical modulation, input-specific short- and long-term synaptic plasticity, neuronal network dynamics, connectivity, and criticality to demonstrate the utility of these organoids in basic science research. Neural organoids showed synapse formation, glutamatergic and GABAergic receptor expression, immediate early gene expression basally and evoked, functional connectivity, criticality, and synaptic plasticity in response to theta-burst stimulation. In addition, pharmacological interventions on GABAergic and glutamatergic receptors and input-specific theta-burst stimulation further shed light on the capacity of neural organoids to mirror synaptic modulation, specifically short- and long-term potentiation and depression, demonstrating their potential as tools for studying neurophysiological and neurological processes and informing therapeutic strategies for diseases.

Neural organoids, which can be grouped under the umbrella term of Brain Microphysiological Systems (bMPS), are derived from human induced pluripotent stem cells (hiPSCs) and offer a powerful tool for studying brain development, disease modeling, drug discovery, and personalized medicine¹⁻². They can recapitulate key features of the human brain, including cellular diversity³⁻⁶, connectivity⁷, and functionality^{3,4,8}, and can capture specific donor genotypes⁹. The model used for this study is comprised of multiple neural cell types, including GABAergic, glutaminergic, cholinergic, serotonergic, and dopaminergic neurons; neural progenitor cells (NPCs),

astrocytes, and myelinating oligodendrocytes^{10,11}. Functional analysis of another neural organoid model has shown that their oscillations are similar to human preterm neonatal EEG features¹². Other neural organoid models have been shown to harbor neuronal assemblies with ample size and functional connectivity, enabling them to collaboratively trigger field potentials⁷. Recently, neural organoids have been proposed as a model of cognition, potentially capable of modeling learning and memory (OI – organoid intelligence)¹³. Although OI as a field, is still in its infancy, the global interest of researchers to develop a model of learning-on-chip for

¹Center for Alternatives to Animal Testing (CAAT), Johns Hopkins University, Baltimore, MD, USA. ²Department of Environmental Health and Engineering, Johns Hopkins University, Baltimore, MD, USA. ³Cortical Labs Pty Ltd, Melbourne, VIC, Australia. ⁴Department of Electrical and Computer Engineering, Princeton University, Princeton, NJ, USA. ⁵Department of Physics and Astronomy, Johns Hopkins University, Baltimore, MD, USA. ⁶Neuroscience Research Institute, University of California Santa Barbara, Santa Barbara, CA, USA. ⁷Department of Molecular, Cellular and Developmental Biology, University of California Santa Barbara, Santa Barbara, CA, USA. ⁸Research and Exploratory Development Department, Johns Hopkins University Applied Physics Laboratory, Laurel, MD, USA. ⁹Department of Biochemistry and Pharmacology, University of Melbourne, Parkville, VIC, Australia. ¹⁰CAAT-Europe, University of Konstanz, Konstanz, Germany. ¹¹Doerenkamp-Zbinden Chair for Evidence-based Toxicology, Department of Environmental Health and Engineering, Johns Hopkins University, Baltimore, MD, USA. ✉e-mail: lena.smirnova@jhu.edu

biomedical research is rapidly growing. For example, organoids were used for reservoir computing, demonstrating spatial information processing and network plasticity as a form of unsupervised learning¹⁴. In addition, goal-directed learning has been successfully performed in organoids¹⁵. The extent to which organoids model the mechanisms of learning and memory needs to be explored further. To develop a reliable OI model, we first need to understand the molecular and cellular machinery of learning, neuronal network activity and function, and synaptic plasticity in neural organoids - an ongoing goal for our group and others.

One critical aspect of brain functionality that is important for learning and memory is synaptic plasticity^{16–19}. Short- and long-term potentiation (S(L)TP) are activity-dependent forms of synaptic plasticity associated with short- and long-term learning and memory processes^{16,20,21}. LTP occurs at the cellular level and involves modifications in synaptic transmission to enhance signal conduction^{16,22,23}. Both LTP and STP are NMDA receptor-dependent forms of synaptic plasticity^{21,24–26}. Synaptic plasticity relies on the rapid activation of immediate early genes (IEGs) in response to stimuli and plays a key role in mediating the transcription and translation of other genes involved in the formation and maintenance of memories²⁷. Altered synaptic plasticity leads to abnormal neural network activity, impairing cognitive functions and behavior, and has been linked to various neurological and psychiatric disorders^{19,28}.

Criticality is another important aspect of neuronal activity that has been shown to optimize the ability of neuronal networks to encode and process information²⁹. At the critical state, neuronal activity exhibits scale-free dynamics, allowing for efficient information processing and integration across different brain regions³⁰. In addition, research has shown that criticality is important for learning and memory in the brain³¹. Research in monolayers of cortical cultures suggests that criticality may be a fundamental property that arises in dynamic systems receiving structured information, making it a valuable metric to assess in more complex cultures³⁰. Likewise, criticality has been observed to vary in response to pharmacological intervention in neural cultures and so can be a highly nuanced metric to consider³². Despite this perspective, aspects of criticality in neural organoids are less explored^{33,34}.

The extent to which hiPSC-derived neural organoids demonstrate features of synaptic plasticity is still being investigated. One study has shown that organoids respond to external electrical signals and maintain elevated neuronal activity short term³³. Another study has shown that assembloids exhibit STP/LTP using patch clamp methods³⁵. Additionally, Zafeiriou et al. showed that neuronal organoids exhibit both short- and long-term changes in network dynamics³⁶. While these are great first steps, more work needs to be done to characterize and better understand synaptic plasticity in neural organoid models.

Here, we focus on analyzing the foundational elements of learning and memory in neural organoids through the characterization of spontaneous and evoked neural network dynamics, input-specific synaptic plasticity, functional connectivity, IEG expression, and criticality. We show that our model has spontaneous and evoked highly interconnected neural networks that change over time, show expression and activation of IEGs, and demonstrate critical dynamics.

Results

Neural organoids were differentiated from iPSC-derived Neural Progenitor Cells (NPC) for up to 14 weeks and characterized throughout development (Fig. 1a). Gene expression of synaptic plasticity markers was quantified from week 0 to week 12. Calcium signaling development was analyzed from week 2 to week 14. Finally, electrical activity was characterized by High-Density Microelectrode Arrays (HD-MEAs) over two independent time periods, from weeks 6-to-9 and 10-to-13. In addition, pharmacological modulation of neurotransmission was performed at weeks 8 and 13. Lastly, input-specific Theta Burst Stimulation (TBS) was implemented at week 14 to induce synaptic plasticity. To analyze both spontaneous and evoked electrical activity from the HD-MEA data, functional connectivity and criticality analysis were performed. A schematic overview of the neurocomputational investigations is shown in Fig. 1b. In addition, an example of how evoked

activity from pharmacological or electrical stimuli can modulate synaptic transmission to induce synaptic plasticity is shown in Fig. 1c. In long-term potentiation, IEGs play a role in trafficking of glutamatergic receptors into the postsynaptic terminal (Fig. 1c), therefore expression of these IEGs can serve as a molecular marker for long-term memory^{27,37}.

Neural organoids develop proper synapse formation and express receptors necessary for synaptic transmission

Neural organoids were differentiated following our in-house established protocol¹¹. The expression of markers for astrocytes (*GFAP*), oligodendrocytes (*MBP*, *OLIG2*) and mature neurons (*MAP2*) increased in the first 8 weeks of maturation and then plateaued in the following weeks, indicating that the differentiation predominantly occurs rapidly until week 8 and then reaches a more stable, mature cell composition from week 8 to 12 (Supplementary Fig. 1). Hence, two time points were selected for the experiments in this paper.

RNA-sequencing (RNAseq) revealed some interesting trends in gene expression between week 8 and week 12/13 organoids. Firstly, while many GABAergic markers showed no difference in expression (e.g., *PVALB*, *GABRA1*, *LHX6*), we observed a slight trend in downregulation of several GABAergic markers, such as *SST*, *SLC32A1*, and *GAD 1* and *2* in the week 12/13 organoids compared to the week 8 group, as shown in Supplementary Fig. 2a and b.

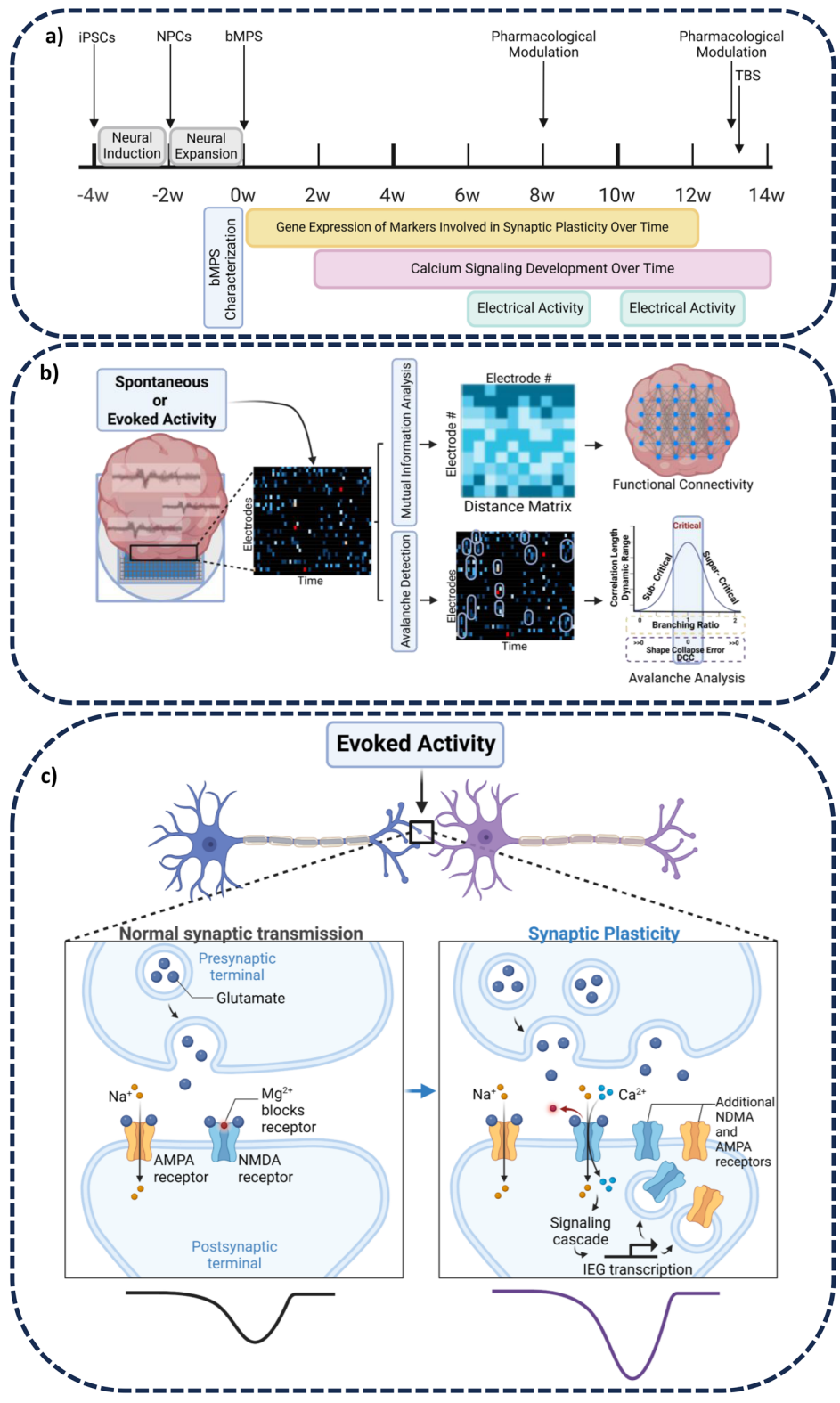
By comparing expression levels across main cell lineages and brain regions (Supplementary Figs. 3 and 4), we observe an increase in the expression of astrocyte markers (e.g., *AQP4*, *GFAP*, *HOPX*, *S100B*, and *SLC1A3*) in the week 12/13 group compared to week 8. These data suggest that the observed trends in downregulation in expression of GABA and glutamatergic markers (*GRIN3A*, *GRIN3B*, and *SLC17A7*) may be linked to the shift in cellular populations with more astrocytes (based on the higher expression of astrocyte markers in the week 12/13 organoids), (Supplementary Figs. 2 and 3). We also profiled the expression of brain region markers, which showed the presence of genes across the forebrain, hindbrain, and midbrain and no consistent differences in expression between the two age groups (Supplementary Fig. 4).

These findings are further supported by the functional enrichment analysis (Supplementary Fig. 5), which revealed that genes associated with synaptic signaling, neuronal differentiation, and axonogenesis were downregulated and cell cycle genes were upregulated in the week 12/13 group (Supplementary Fig. 5).

We then evaluated the presence of pre- and postsynaptic markers as well as IEGs as the key proteins involved in synaptic plasticity and learning formation. Presence of the presynaptic marker Synaptophysin (SYP) and postsynaptic marker HOMER1 was detected in both week 8 and 12 organoids, displaying typical punctual staining (Fig. 2a). Gephyrin-positive signal was close to background with few positive cells at week 8 and increased at week 12 (Fig. 2b). This indicates that there are more developed inhibitory synapses at the later stage of differentiation. Gene expression of *GABRA1*, which encodes the inhibitory GABA_A receptor, followed the same pattern (Fig. 2c). Gene expression of postsynaptic marker *HOMER1* was steady over time (Fig. 2c). Presence of Synapsin1 and MAP2 seemed to be reduced at week 12 vs. week 8, supporting RNAseq data of the lineage shift towards more astrocytes (Fig. 2b), although cell number quantification is needed to drive the final conclusions.

Both AMPA and NMDA receptors play an important role in synaptic plasticity, including STP/LTP^{24,38,39}, therefore showing expression of these receptors was imperative for this study to give insight into the mechanisms of learning and memory in neural organoids. The increase in gene expression over time was the greatest for *GRIN1*, which plateaued around week 8 to week 12 (Fig. 2c). *GRIN2A* and *GRIN2B* both increased over time with a higher increase of *GRIN2A* expression than *GRIN2B*, suggesting increasing maturity⁴⁰ (Fig. 2c). *GRIA1* expression also increased over time and plateaued after week 8 (Fig. 2c). Thus, plateau in expression of these subunits suggests the organoids reached a mature state between week 8 to 12.

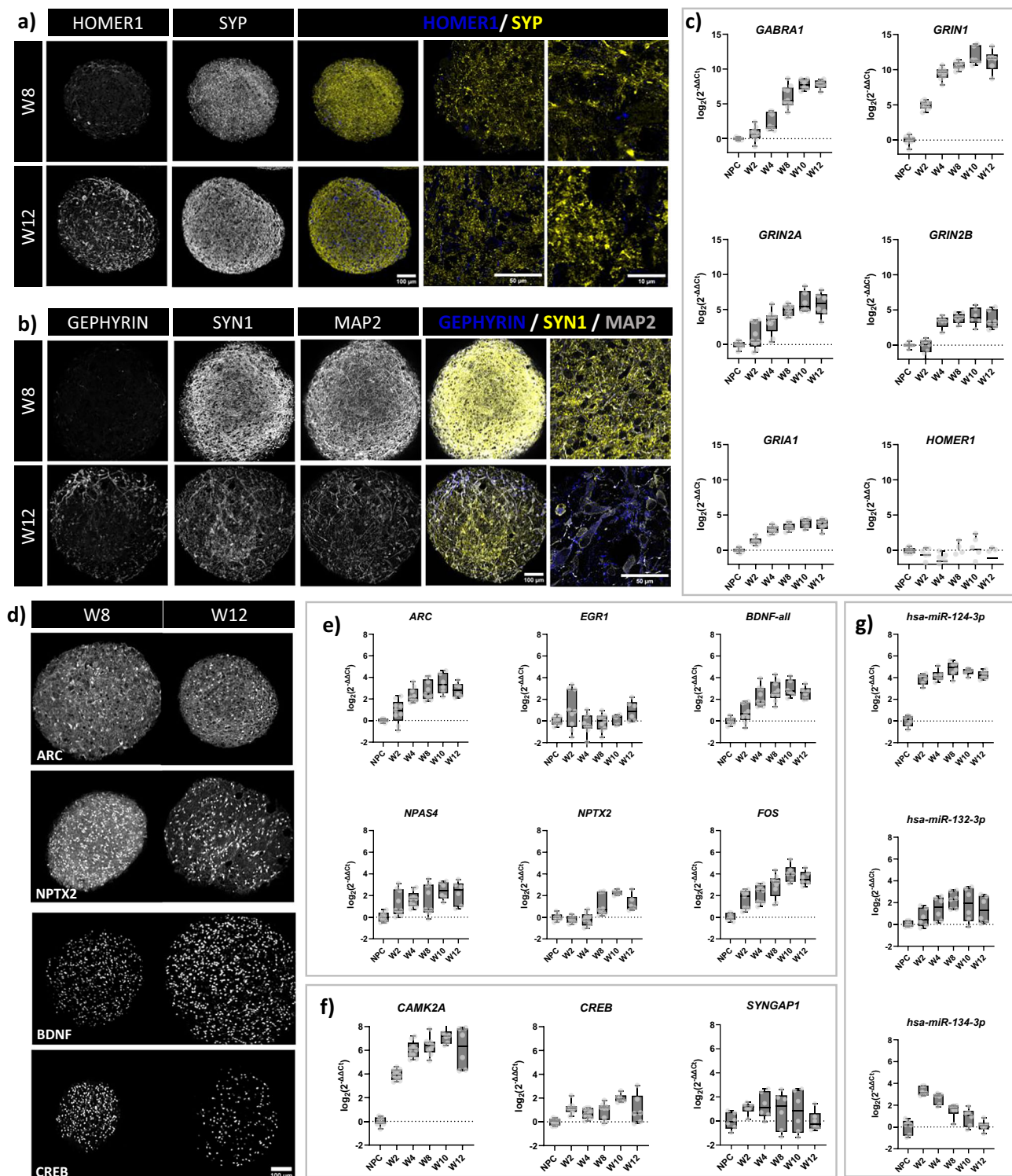
Fig. 1 | Schematic overview of the experimental approach. **a** Experimental timeline. Created in BioRender. Alam El Din, D. (2025) <https://BioRender.com/v4k2lpz> **b** Overview of avalanche and network connectivity analysis for time series electrophysiology data from organoids plated on HD-MEAs. Created in BioRender. Alam El Din, D. (2025) <https://BioRender.com/trj7ehf> **c** Schematic representation of synaptic transmission modulation by pharmacological and electrical stimuli to induce synaptic plasticity. Adapted from Kim, S. (2025). Long-Term Potentiation. <https://app.biorender.com/biorender-templates/details/t-61006a6924e0d000a40de3a1-long-term-potentiation>. Created in BioRender. Alam El Din, D. (2025) <https://BioRender.com/eqpwhdw>.



Dynamic expression of immediate early genes associated with synaptic plasticity and cognitive functions over time

IEGs are crucial for cognitive functions as they act directly at the synapse and mediate the cellular processes that are essential for learning and memory consolidation²⁷. To demonstrate that the neural organoids have the necessary cellular components for cognitive processes, we quantified IEG expression during the course of differentiation (Fig. 2d, e, Supplementary Fig. 6). Gene expression of *ARC*, *BDNF*, *NPAS4*, *NPTX2*, and *FOS* was

significantly increased over time, while *EGR1* was already expressed in NPCs and remained at levels close to those in NPCs. Expression of upstream regulators of IEGs (*CREB* and *CAMK2A*) also increased over time with the largest increase in expression of *CAMK2A* (Fig. 2f). In addition, *SYNGAP1*, which plays a key role in regulating synaptic function and plasticity⁴¹, was stably expressed throughout the course of differentiation, starting from NPCs. The levels of IEG proteins (*NPTX2*, *ARC*, and *BDNF*) and upstream IEG transcription factor *CREB* were comparable between week 8 and 12,



confirming the plateau observed in RT-qPCR data (Fig. 2d). These results were consistent with RNAseq data which showed no changes in IEG expression between 8 and 12/13 week old organoids (Supplementary Fig. 6a and Supplementary Fig. 6b).

Finally, we assessed the expression of microRNAs known to be involved in synaptic plasticity (Fig. 2g)⁴² and observed expected dynamics. A strong increase in expression of *mir-124-3p* over the course of differentiation was observed. *mir-132-3p* and *mir-134-3p* had opposite expression patterns: *mir-132-3p* was increased over time while expression of *mir-134-3p* was first

strongly induced from NPC to 2 weeks of differentiation and was down-regulated thereafter (Fig. 2g).

Evidence of spontaneous electrical activity and highly interconnected neuronal networks in neural organoids

Electrophysiology over the course of organoid development was characterized using calcium imaging and HD-MEAs. In addition to the expression of molecular machinery involved in synaptic plasticity, neural organoids showed highly patterned spontaneous electrical activity

Fig. 2 | Expression of glutamatergic and GABAergic receptor and synaptic plasticity-related genes in neural organoids over course of differentiation.

a Representative immunocytochemistry images of organoids showing postsynaptic marker (HOMER1) and presynaptic marker (SYP) in 8- and 12-week cultures. In composite images, HOMER1 is shown in blue, and SYP is shown in yellow. Scale bars are 100 μ m, 50 μ m, and 10 μ m, respectively. **b** Presence of inhibitory post-synaptic marker (Gephyrin), pre-synaptic marker (SYN1) and dendrites (MAP2) in 8- and 12-week organoids. In composite images, Gephyrin is shown in blue, SYN1 in yellow, and MAP2 in grey. Scale bars are 100 μ m and 50 μ m, respectively. For **a**, and **b**, all images were taken at 20x, 100x, and 100x + 4x zoom and processed with ImageJ for visualization. **c** Gene expression of Gamma-Aminobutyric Acid Type A Receptor Subunit Alpha1 (*GABRA1*), Glutamate Ionotropic Receptor NMDA Type Subunit 1 (*GRIN1*), Glutamate [NMDA] Receptor Subunit Epsilon-1 (*GRIN2A*), and Glutamate [NMDA] Receptor Subunit Epsilon-2 (*GRIN2B*), Glutamate Ionotropic Receptor AMPA Type Subunit 1 (*GRIA1*), homer scaffold protein 1

(*HOMER1*) in organoids over the course of differentiation. **d** Representative immunocytochemistry images of weeks 8 and 12 organoids stained for Neuronal Pentraxin 2 (NPTX2), Activity-Regulated Cytoskeleton-associated protein (ARC), cAMP response element-binding protein (CREB), and Brain-Derived Neurotrophic Factor (BDNF). Scale bar is 100 μ m. **e** Gene expression over the course of differentiation of immediate early genes (IEGs) *ARC*, *BDNF*, Neuronal PAS Domain Protein 4 (*NPAS4*), *NPTX2*, Fos proto-oncogene AP-1 transcription factor subunit (*FOS*), and Early Growth Response 1 (*EGR1*). **f** Gene expression of synaptic plasticity-related genes: *CREB*, calcium/calmodulin-dependent protein kinase II A (*CAMK2A*), Synaptic Ras GTPase-activating protein 1 (*SYNGAP1*). **g** Gene expression of synaptic plasticity-related miRNAs. For all gene expression plots, data is shown as a box and whisker plot (with the box extending from the 25th to 75th percentiles) and represented as log₂(Fold Change) normalized to NPCs from 2-3 independent experiments with 3 technical replicates each. In all qPCR experiments, *ACTB* was used as a reference gene.

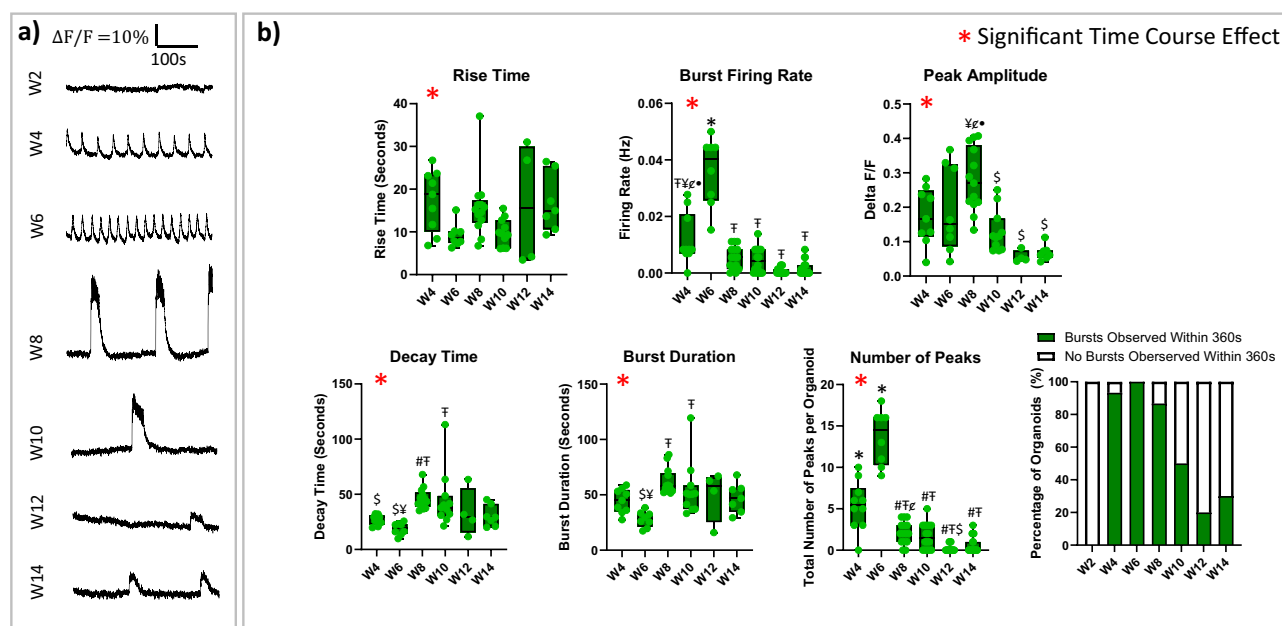


Fig. 3 | Neural organoid calcium oscillatory dynamics across different time points to show maturation of spontaneous network bursting. a Representative changes in fluorescence over resting fluorescence ($\Delta F/F$) graphs across 360 seconds for each time point from week 2 (W2) to week 14 (W14) of differentiation. **b** Average rise time, peak amplitude, firing rate, decay time, burst duration, number of peaks, and percentage of active organoids shown across different time points. At least 8 individual organoids across at least 3 independent experiments were imaged and quantified for each time point. Data is shown as box and whisker plots (with the box extending from the 25th to 75th percentiles). Statistics were performed using one-way

ANOVA and a Tukey post-hoc test. Changes over time were significant for rise time ($p < 0.05$), burst firing rate ($p < 0.0001$), peak amplitude ($p < 0.0001$), decay time ($p < 0.01$), burst duration ($p < 0.001$), and total number of peaks per organoid ($p < 0.0001$). Pairwise comparisons are shown on the figure: # = Significant difference from week 4, T = Significant difference from week 6, S = Significant difference from week 8, ¥ = Significant difference from week 10, ε = Significant difference from week 12, • = Significant difference from week 14, * = Significant difference from all weeks. For exact p values see Supplementary Tables 4–9. See also Supplementary Fig. 7 for single neuron calcium imaging analysis.

(Figs. 3 and 4). Calcium transients were measured using Fluo-4 biweekly from week 2 to 14. Whole organoid change in fluorescence over resting fluorescence intensity ($\Delta F/F$) was quantified and compared across age groups (Fig. 3a). From these $\Delta F/F$ plots, the average rise time, peak amplitude, firing rate, decay time, burst duration, number of peaks, and percentage of active organoids per time point were calculated (Fig. 3b). Bursts were identified as peaks in calcium transients. Burst firing rate was calculated as the number of burst peaks per second.

Calcium imaging showed that 2-week-old organoids did not exhibit spontaneous oscillatory calcium dynamics. The first signs of oscillatory calcium activity were detected at week 4, with high-frequency oscillations at weeks 4 and 6, as shown by higher burst firing rates and number of peaks (Fig. 3, Supplementary Video 1, and Supplementary Fig. 7). At week 8, oscillation patterns shifted to lower frequency with fewer calcium peaks, lower burst firing rates, higher amplitudes, longer burst durations, and larger decay times (Fig. 3, Supplementary Video 2, and Supplementary

Fig. 7). The plateau shape of the oscillations at week 8 indicated multiple neuronal action potentials contributing to the calcium oscillation (Fig. 3a). The decrease in the number of peaks from weeks 6 to 8 suggested more synchronous calcium transients, indicating a more densely connected mature network. From weeks 10 to 14, burst duration, decay time, and number of peaks did not change significantly, but amplitude and percentage of active organoids decreased, suggesting a plateau in differentiation around week 8.

In addition to whole organoid analysis, $\Delta F/F$ was quantified in single neurons for at weeks 4–10 (Supplementary Fig. 7). Maximum intensity z-projections of time course videos showed that neuronal networks at weeks 4 and 6 were less connected compared to weeks 8 and 10 (Supplementary Fig. 7). At weeks 4 and 6, neurons spiked at higher frequencies and with less synchronization (Supplementary Fig. 7a and b). By weeks 8 and 10, larger burst amplitudes and longer burst durations are likely contributed to multiple action potentials across different neurons, which were spiking

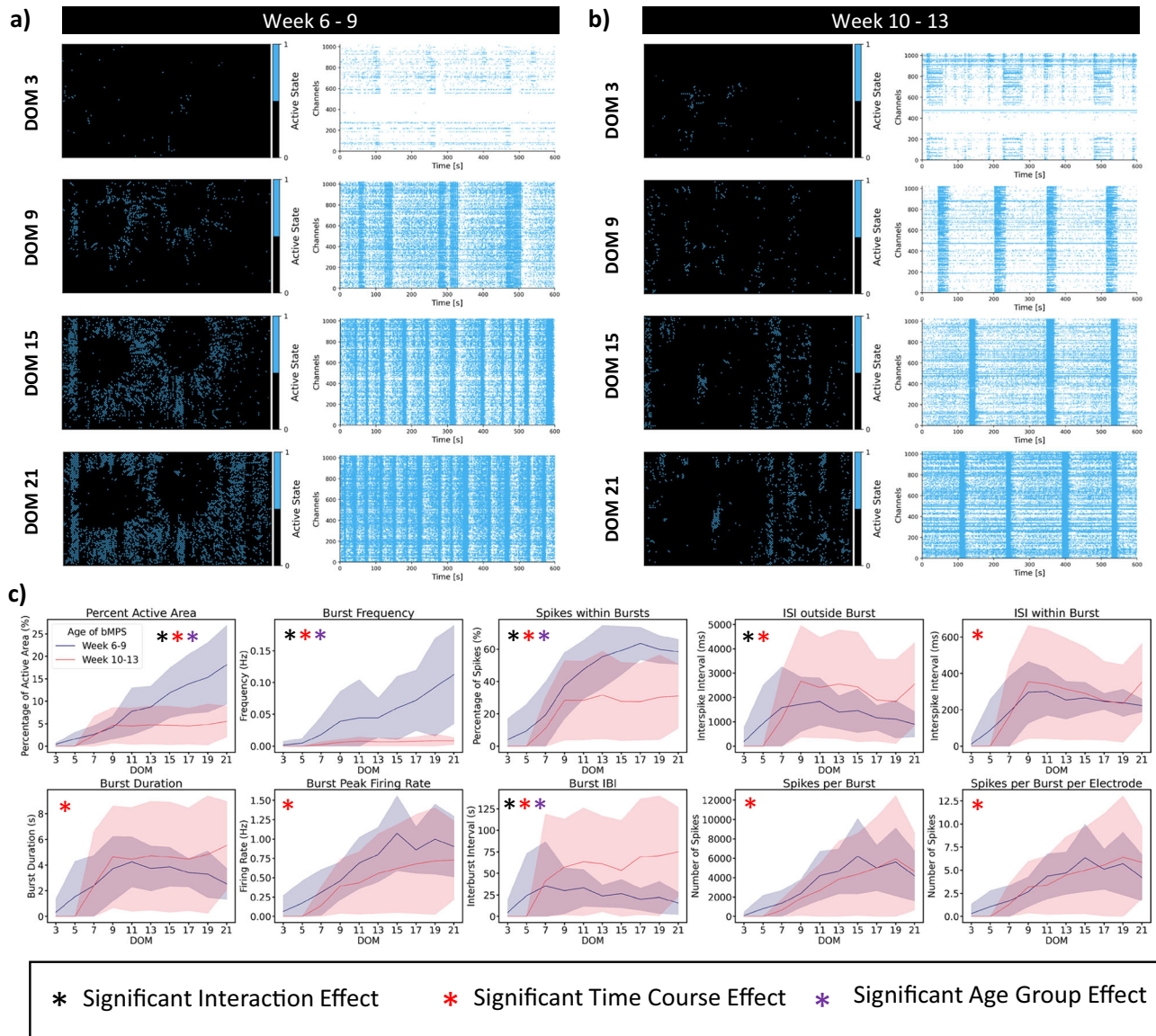


Fig. 4 | Changes in spontaneous electrical activity in neural organoids throughout development. Representative raster plots and active area plots from HD-MEA recordings showing spontaneous electrical activity over time during **a** weeks 6-to-9 and **b** weeks 10-to-13 of differentiation. DOM: Days on MEAs. **c** Network dynamic metrics from both organoid age groups over time (blue line represents 6-to-9 week organoids, red line – 10-to-13 week organoids). The line shown represents mean and the shaded region represents the standard deviation

plotted from 2 independent experiments with 5 to 6 HD-MEA wells per experiment with 2–5 organoids per well ($n = 11-12$ wells per age group). Statistics were performed using a mixed-effects model with matching and a Tukey post-hoc test. $p < 0.05$ was considered significant. For exact p values from pairwise comparisons, see the Supplementary Data 3 file. ISI: Interspike Interval. IBI: Interburst Interval.

simultaneously (Supplementary Fig. 7c and d). At week 10, the propagation of an action potential across connected neurons was observed by the slightly delayed peak burst amplitude of region of interest (ROI) 1 compared to ROIs 2 and 3 (Supplementary Fig. 7d).

To measure network activity over time, HD-MEAs were used to obtain high spatial and temporal resolution of organoids' electrical activity across two different time periods (weeks 6-to-9 and 10-to-13) (Fig. 4). Representative raster plots indicated differences in spontaneous electrical activity in organoids depending on their age (Fig. 4a, b). The 6-to-9-week organoids have a significantly higher burst frequency, number of spikes within burst, and percent active area than those in the later time point group (Fig. 4c). They also had significantly shorter interburst intervals compared to the more mature group, consistent with the calcium imaging data in Fig. 3.

To further assess the organoids' functionality, neuronal connectivity and criticality were quantified from the same HD-MEA time course data

(Figs. 5 and 6). In both age groups, changes in functional connections between electrodes were observed over time on the HD-MEA (Fig. 5a). Denser connections and more active electrodes were observed in the 10-to-13-week group compared to the 6-to-9-week group, as denoted by the thickness of the black lines and red electrodes, respectively in the connectivity graphs (Fig. 5a). However, while both groups showed significant increases in the number of nodes over time, the 10-to-13-week group had a significantly lower number of nodes overall in their functional connectivity matrices compared to the 6-to-9-week group (Fig. 5b). To quantify the shift in the strength of the edges over time, an edge weight distribution was calculated by measuring the fraction of total possible edges that are realized (Fig. 5c). Interestingly, most edges were activated across all samples over time (Fig. 5c). The 10-to-13-week group showed no significant changes over time, while the 6-to-9-week group showed a temporary significant decrease in strength of edges at day on MEA (DOM) 7 (Fig. 5c). Finally, the organoid's modularity was significantly different across age groups and

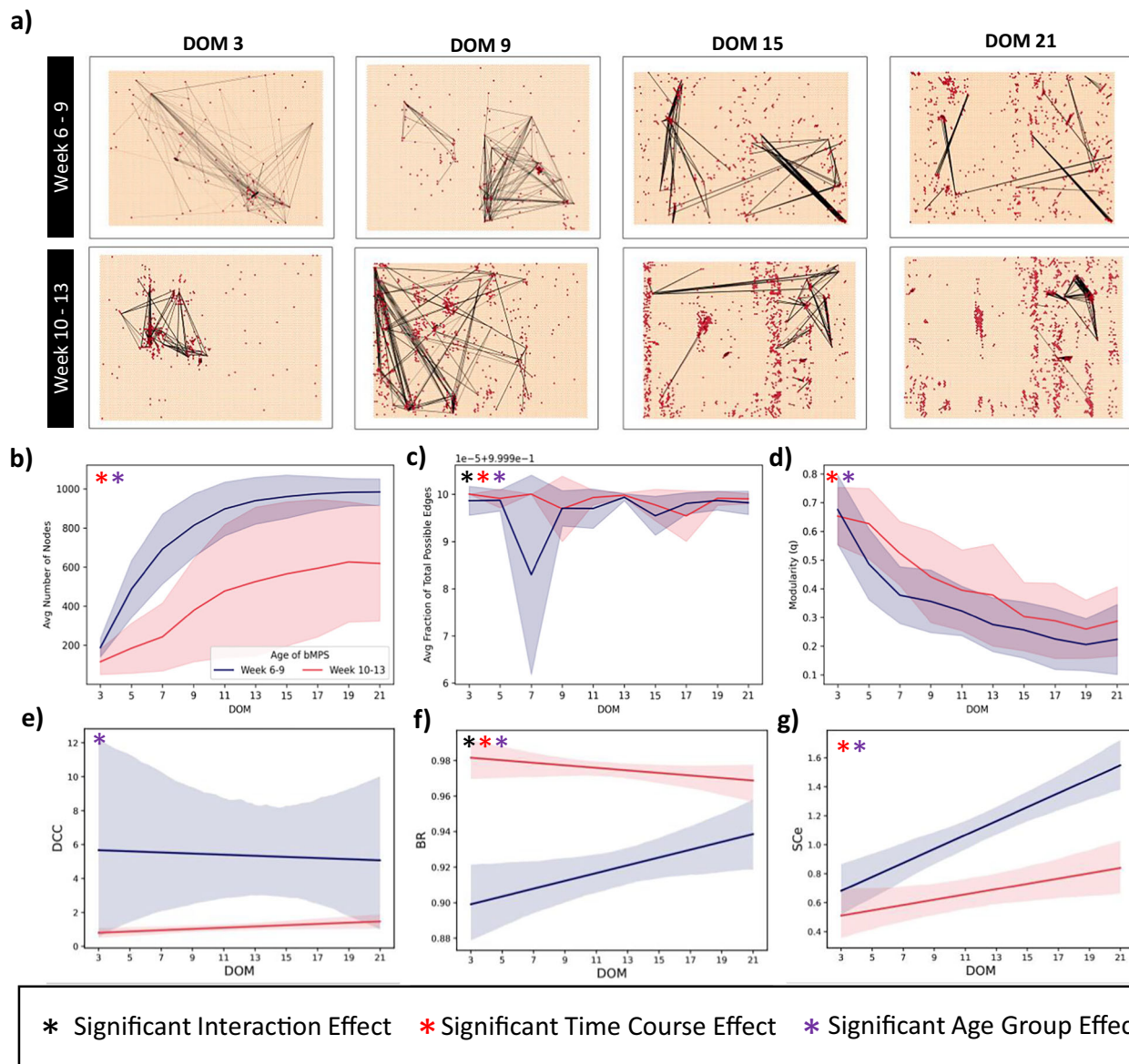


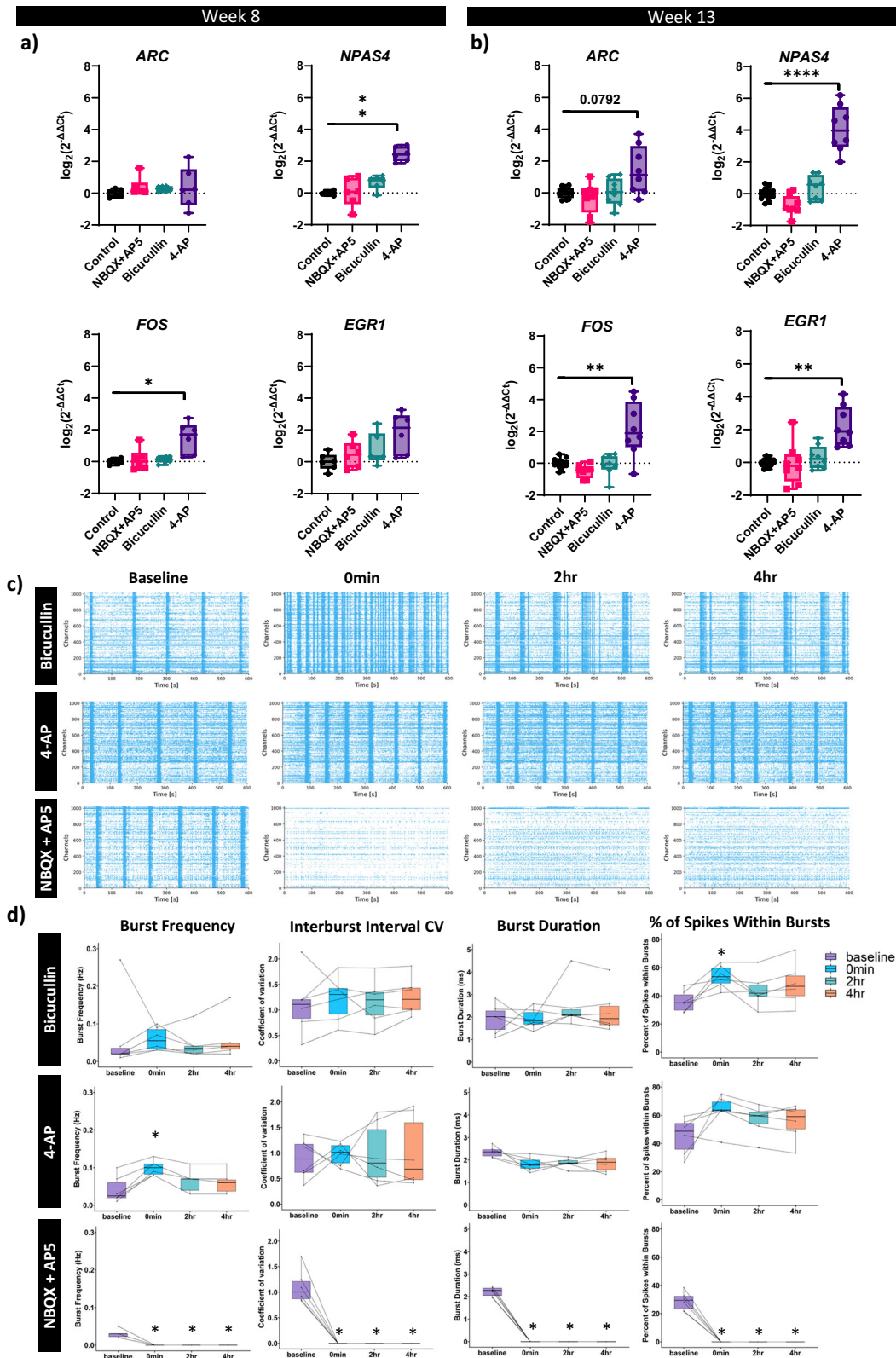
Fig. 5 | Neural organoids show highly interconnected neuronal networks and criticality throughout development. **a** Representative plots of functional connectivity at day on MEA (DOM) 3, 9, 15, and 21 for the week 6-to-9 and week 10-to-13 old organoids. For clarity of visualization, only the 200 connections (edges) with the highest mutual information are shown. Each red dot represents an electrode, and the lines indicate the connections between electrodes. The thickness of the line indicates the weight of connectivity. **b** Average number of nodes; **c** Average fraction of total possible edges; **d** Average modularity over time in week 6-to-9 and week 10-to-13 organoids. **e** Deviation from Criticality Coefficient (DCC). **f** Branching Ratio (BR) **g** Shape collapse error (SCe) over time in 6-to-9 week and 10-to-13 week old

organoids. In **b–d** the line shown represents the mean and the shaded region represents the standard deviation plotted from 2 independent experiments with 5 to 6 HD-MEA wells per group per experiment with 2–5 organoids per well ($n = 11–12$ wells per age group). Panels **e–g** show regression lines (blue line - 6–9 week old organoids, red line - 10–13 week old organoids) with a 95% confidence interval. Data plotted is from 2 independent experiments with 5–6 HD-MEA wells per group per experiment ($n = 11–12$ wells per age group). Statistics were performed using a two-way ANOVA and a Tukey post-hoc test. $p < 0.05$ was considered significant. For exact p values from pairwise comparisons, see the Supplementary Data 3 file.

significantly decreased in both age groups over time, indicating that the networks started with multiple communities but then became more of a single community over time (Fig. 5d). The decrease in modularity may also be due to an increased number of nodes. Despite the similarity in modularity, the 10-to-13-week group maintained a significantly higher modularity over time, indicating that it maintained more communities or network connections (Fig. 5d).

Criticality is a state in which complex systems such as a brain operates at the critical point between organization and randomness, demonstrating how neuronal networks may navigate between the two stages of chaos and order⁴³. The critical point state is key for brain functionality, as it operates at its optimal and most efficient computational capacity and is highly

sensitive to external stimuli during this stage. Organoids exhibited properties of criticality over the course of differentiation (Fig. 5e–g). The more mature 10-to-13-week group showed a consistently lower and more tightly regulated Deviation from Criticality Coefficient (DCC) value and higher Branching Ratio (BR), approaching 1, compared to the 6-to-9-week group (Fig. 5e). While the BR in the 10-to-13-week group decreased non significantly over the period of 3 weeks on the HD-MEAs, the 6-to-9-week group gradually increased significantly, demonstrating maturation and pursuit of criticality and thus a stable state (Fig. 5f). Additionally, the Shape Collapse error (SCe) for the 10-to-13-week group was significantly lower than that of the 6-to-9-week group, indicating a more accurate scaling of avalanches of varying durations to a universal shape in the



10-to-13-week group (Fig. 5g). This analysis suggests that the 10-to-13-week group was in a more critical state compared to the 6-to-9-week group. However, over time, both the BR and SCell appeared to converge for both groups, suggesting that the 6-to-9-week group exhibited increasingly critical dynamics, while the 10-to-13-week group showed diminishing critical dynamics on the MEA over time.

Pharmacological characterization of synaptic transmission changes neuronal bursting activity and immediate early gene expression

To validate reactivity to network modulations, pharmacological agents were used to cause neuronal depolarization and disrupt excitatory glutamatergic synaptic transmission. Expression of IEGs and synaptic plasticity-

Fig. 6 | Pharmacological characterization of synaptic transmission changes of neuronal spiking and bursting activity and Immediate Early Gene expression. Expression of *ARC*, *NPAS4*, *FOS*, and *EGR1* after 2 hours of exposure to 20 μ M AP5 + 20 μ M NBQX (pink box), 10 μ M bicuculline (green box) and 100 μ M 4-AP (purple box) in **a** 8-week and **b** 13-week-old organoids, represented as box and whisker plots (25th to 75th percentiles) and as log₂(Fold Change) normalized to negative control (organoids with no chemical treatment = 2 h control). *ACTB* was used as a reference gene. The data represents 3 independent experiments with 2 technical replicates each for 8 weeks and 4-5 independent experiments with 2 technical replicates each for the 13-week time point. Statistics were calculated based on the replicate average from each independent experiment, with one-way ANOVA and post-hoc Dunnett's tests * $p < 0.05$, *** $p < 0.001$, **** $p < 0.0001$. **c** Representative raster plots from MEA recordings in 13-week-old organoids (from 6 wells per condition) before and after treatment with bicuculline, 4-AP, and

NBQX + AP5. **d** Burst frequency, Interburst interval coefficient of variation, burst duration, and percentage of spikes within bursts plotted as box and whisker plot (with the box extending from the 25th to 75th percentiles) for bicuculline, 4-AP, and NBQX + AP5 treated wells prior to (baseline), 0 mins, 2 hours, and 4 hours after exposure. The data represents 3 independent experiments with 2 HD-MEA wells per experiment per chemical ($n = 6$). Statistical significance was calculated with repeated measures ANOVA with post-hoc Dunnett tests. $p < 0.05$ was considered significant. Pairwise comparisons can be seen in the Supplementary Tables 10-21 and significant groups are shown in the figure. *ARC* - Activity-Regulated Cytoskeleton-Associated Protein; *NPAS4* - Neuronal PAS Domain Protein 4; *FOS* - Fos proto-oncogene AP-1 transcription factor subunit; *EGR1* - Early Growth Response Protein 1; AP5 - 2-Amino-5-phosphonopentanoic acid (an NMDA receptor antagonist); NBQX - 2,3-dihydroxy-6-nitro-7-sulfamoyl-benzo[f]quinoxaline (an AMPA receptor antagonist).

related genes was measured 2 hours after exposure to pharmacological agents and compared to the corresponding untreated control in two age groups (8 weeks and 13 weeks) (Fig. 6). To disrupt excitatory glutamatergic synaptic transmission, organoids were treated with 2,3-dioxo-6-nitro-7-sulfamoyl-benzo[f]quinoxaline (NBQX), an AMPA receptor antagonist, D-2-amino-5-phosphonovalerate (AP5), a NMDA receptor antagonist, 4-Aminopyridine (4-AP), a voltage-gated potassium (Kv) channel antagonist, and bicuculline, a GABA receptor antagonist, were used to enhance neuronal depolarization and synaptic transmission (Fig. 6).

Bicuculline induced a slight increasing trend in gene expression across both age groups (Fig. 6a), while exposure to 4-AP led to significant changes in *NPAS4* and *FOS* expression at both age groups. Expression of *ERGI* was significantly induced only at week 13. Lastly, *ARC* expression showed an increased trend in expression after 4-AP exposure (Fig. 6a). No significant changes in gene expression were seen after exposure to NBQX and AP5 individually or combined (Fig. 6 and Supplementary Fig. 8a-d). Since IEGs were more strongly perturbed at week 13, the effects of these chemicals on electrophysiological activity were assessed in this age group. Organoids were exposed to the pharmacological agents directly on the HD-MEA at DOM 29. Network recordings were taken before the addition of the chemicals as a baseline. Network activity was then recorded immediately after exposure, followed by 2 and 4 hours thereafter, after which the recorded parameters were compared to baseline activity (Fig. 6c and d). 4-AP and bicuculline increased network activity while NBQX + AP5 decreased network activity over time (Fig. 6c). More specifically, bicuculline caused an insignificant increasing trend in mean burst frequency and interburst interval coefficient of variation (CV) over time, a significant increase in percent of spikes within bursts 0 minutes after and an increasing trend in percent of spikes within bursts 2 and 4 hours after exposure. In addition, bicuculline caused no significant changes or trends in burst duration over time. 4-AP exposure caused a significant increase in mean burst frequency and an increasing trend in mean percent of spikes within bursts 0 minutes after. In addition, the percentage of spikes within bursts maintained an increasing trend within 2 and 4 hours after exposure. 4-AP also caused a decreasing trend in burst duration that was maintained over time. Finally, 4-AP caused no significant changes or trends in interburst interval CV over time. Additionally, NBQX + AP5 exposure completely abolished network bursting activity (Figs. 6c and d, Supplementary Fig. 8). Overall, NBQX + AP5 significantly decreased mean burst frequency, interburst interval CV, burst duration, and percentage of spikes within bursts from 0 minutes to 4 hours. Interestingly, we found that NMDA receptors are largely responsible for neuronal network bursting, as exposure to only AP5 was enough to abolish the bursting, while blocking only AMPA receptors with NBQX only partially reduced the bursting (Supplementary Fig. 8). These results agreed with previous reports showing that ketamine and xenon, which act on NMDA receptors, lead to burst silencing and reduction in vitro^{44,45}. No changes in firing rate, spikes per burst, and burst duration were seen after NBQX application alone, but when AP5 or NBQX + AP5 was applied, no bursts were observed; therefore, firing rate, spikes per burst, and burst duration were not quantifiable (Supplementary Fig. 8).

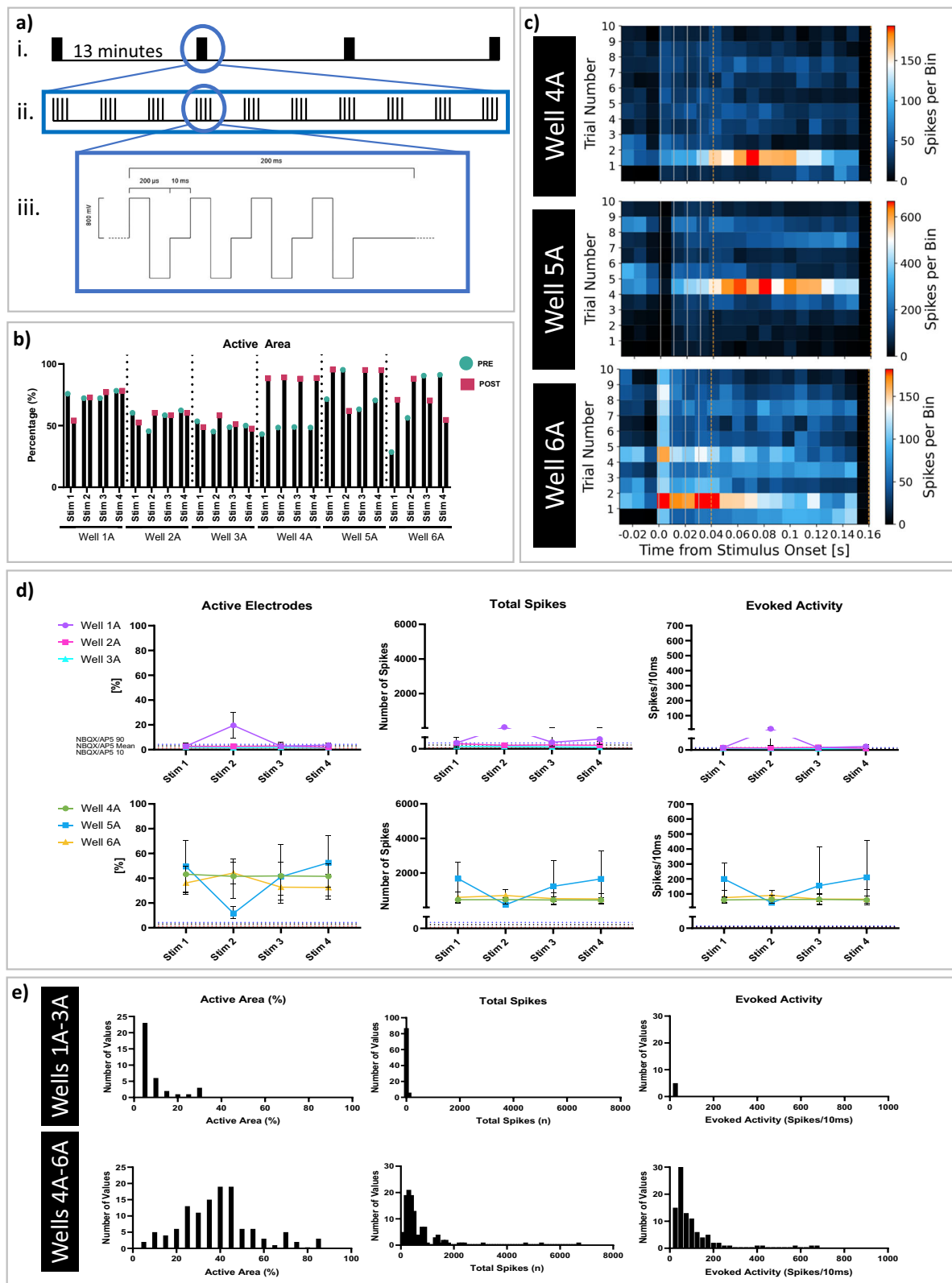
While NBQX + AP5 reduced the network bursting, some spiking activity was still seen (Fig. 6c and Supplementary Fig. 8e). To elucidate which type of neurons contributed to the remaining activity, different modulators of the glutamatergic, GABAergic, dopaminergic, noradrenergic and cholinergic neurons were tested in different combinations (Supplementary Fig. 9). The first set of experiments further blocked NMDA and AMPA receptors, by increasing concentrations of NBQX + AP5 to 40 μ M. As for the previous 20 μ M exposure (Fig. 6c and Supplementary Fig. 8e), all bursting was abolished and spiking was diminished, but increased concentration did not remove the activity completely. Therefore, next, we blocked different types of neurons. First, 10 μ M bicuculline and 10 μ M CPG 55845 hydrochloride (CPG 55845) were added to block GABA(A) and GABA(B) receptors in addition to NMDA and AMPA receptors. Upon addition of bicuculline and CPG 55845, a further reduction in spiking activity was observed (Supplementary Fig. 9a, last panel, 10-20 min). The quantification of the effect after blocking excitatory receptors and the subsequent blocking of inhibitory neurons is shown in Supplementary Fig. 9d.

Next, inhibitory and excitatory receptors were blocked simultaneously by adding 40 μ M NBQX, 40 μ M AP5, 10 μ M bicuculline, and 10 μ M CPG 55845 at the same time with similar effects as before (Supplementary Fig. 9b). Subsequently, 5 μ M 6-hydroxydopamine (6-OHDA) and 10 μ M haloperidol were added, which induce lesions in dopaminergic (and noradrenergic) neurons and block dopamine D2 receptors, respectively. This resulted in an even more pronounced reduction in spiking activity (Supplementary Fig. 9b, the last panel). Supplementary Fig. 9e quantifies the corresponding changes in bursting and spiking metrics. These results suggest that most of the remaining activity originated from dopaminergic and noradrenergic neurons.

The last population of neurons examined for chemical modulation effects was cholinergic neurons. To achieve this, 40 μ M NBQX, 40 μ M AP5, 10 μ M bicuculline, 10 μ M CPG 55845, 5 μ M 6-OHDA, and 10 μ M haloperidol were added simultaneously to block excitatory, inhibitory, dopaminergic and noradrenergic neurons. The same effect as shown in Supplementary Fig. 9b was also observed in Supplementary Fig. 9c, demonstrating a drastic reduction in bursting and spiking, as quantified in Supplementary Fig. 9f. Finally, 1 nM chlorpyrifos (CPF)-Oxone was added to that same well to attempt to increase activity in the network by activating cholinergic neurons. However, no changes in bursting or spiking were observed, as shown in Supplementary Fig. 9c and quantified in Supplementary Fig. 9f. Therefore, findings suggest that the remaining activity likely originated from partially blocked AMPA and NMDA receptors, as well dopaminergic and noradrenergic neurons.

Theta-burst stimulation modulated synaptic plasticity

To generate input-specific evoked activity from electrical stimulation, Theta Burst Stimulation (TBS) was delivered to 14-week-old organoids 4 times with 13-minute intervals between TBS (Fig. 7a) on the HD-MEA. Two independent experiments (referred to as A and B in the figures and below) were conducted. In both experiments, four to five organoids were seeded on each well at week 9.5 of differentiation and grown on the MEA until 33 ± 1



DOM before stimulation (Supplementary Fig. 10a and Supplementary Fig. 11a). First, we recorded the baseline network activity across all wells and found that basal activity was lower in wells 1A-3A than wells 4A-6A and 1B-4B (Supplementary Figs. 10b and 11b). The MaxWell HD-MEA has an electrode size of $8.75 \times 12.50 \mu\text{m}^2$, and the electrode center-to-center distance is $17.5 \mu\text{m}$, allowing one neuron to be recorded by multiple electrodes.

For input-specific synaptic plasticity, one neuron from each well was identified based on its footprint (Supplementary Figs. 12a and 13a) and spike-sorted neuron traces using the Axon Tracking assay in the MaxLab Live Software (Supplementary Figs. 12b and 13b). Then, 32 electrodes focusing on a single neuron in each well were stimulated using a modified version of previously described LTP induction protocols⁴⁶⁻⁴⁸ (Fig. 7a).

Fig. 7 | Theta-burst stimulation modulated short-term plasticity for

Experiment A. **a** Graphical summary of TBS protocol. i-The TBS was performed four times spaced by 13 minutes. ii-Within each TBS there are 10 trials with four spikes per trial. iii-The schematic of each trial. **b** Percent active area before and after stimulation across all 6 wells. Wells 4A–6A show consistent increase or decrease in active area in response to stimulation while wells 1A–3A show little change. **c** Representative heat map evoked activity response for wells 4A–6A. Bin size is equal to 10 ms. The stimulation pulses are the light grey vertical lines, and the dashed orange lines indicate the start/stop time of the analysis window for calculating evoked activity. **d** percentage of active electrodes, total spikes, and evoked activity for wells 1A-3A and then 4A-6A. Purple circle represents well 1A, pink square – well 2 A, turquoise triangle – well 3A, green circle – well 4A, blue square – well 5A, and yellow triangle – well 6A. The data represents the mean with 10th to 90th percentile for

each well. The 90th percentile response of a well treated with NBQX/AP5 before and during stimulation is shown with a blue dashed line overlaid on all graphs. The mean response of a well-treated with NBQX/AP5 before and during stimulation is shown in a black dashed line overlaid on all graphs. The 10th percentile response of a well treated with NBQX/AP5 before and during stimulation is shown in a red dashed line overlaid on all graphs. Responses above this NBQX/AP5 region indicate responses generated by glutamatergic receptors. **e** Histograms of total evoked activity per bin (bin size of 10 ms), total spikes, and total active area. The top three graphs show data aggregated across all electrodes for all 4 TBS for wells 1A–3A, and the bottom three graphs show data aggregated across all electrodes for all 4 TBS for wells 4A–6A. Wells 1A–3A show little to no response while wells 4A–6A indicate evoked responses on the millisecond timescale.

To optimize the stimulation of each neuron, electrodes along the entire neuron including the soma and axon were targeted for stimulation.

To investigate short-term changes in evoked activity, total evoked activity per bin (10 ms), total spikes, and total active area were measured. Active area before and after each stimulation are shown for all wells in both experiments (Fig. 7b and Supplementary Fig. 14a). Wells 4A–6A, 1B–4B showed substantial changes in active area in response to the stimulus while wells 1A–3A showed little changes (Fig. 7b, Supplementary Fig. 14a).

Representative evoked activity heatmaps from wells 4A–6A and 1B–4B demonstrated strong short-term responses within milliseconds following stimulation (Fig. 7c, Supplementary Figs. 15, and 16). Wells with lower baseline activity (e.g., 1A–3A) did not show any response.

To determine an activity threshold, we treated one well with NBQX/AP5 to block glutamatergic receptors-dependent synaptic plasticity. The 90th, mean, and 10th percentile responses from the NBQX/AP5-treated well is shown overlaid on the plots as the dotted blue, black, and red lines, respectively (Fig. 7d, Supplementary Fig. 14c). Wells 1A–3A did not exceed this threshold, while wells 4A–6A and 1B–4B consistently did across all four TBS sets (Fig. 7d, Supplementary Fig. 14c).

Aggregated data for active area, total spikes, and evoked activity showed that wells 4A–6A and 1B–4B had a distribution skewed to the right of 0, while wells 1A–3A only exhibited a mode around 0 (Fig. 7e, Supplementary Fig. 14d). Wells 1A–3A, with lower baseline activity and connectivity compared to wells 4A–6A and 1B–4B, did not respond above threshold, whereas the shift to the right of 0 in wells 4A–6A and 1B–4B suggests short-term potentiation, as stimulation led to short-term increases in activity.

To further confirm STP, connectivity and criticality was quantified across each TBS for well that exhibited STP (Well 4A, 5A, 6A, 1B, 2B, 3B, 4B) across both experiments (Fig. 8a–c). We observed a significant increase in the number of nodes and edges while modularity significantly decreased after every stimulation indicating a more connected network of neurons after stimulation (Fig. 8a and b). These results suggest that wells that exhibit evoked electrical activity also became more connected, more of a single community. While metrics of connectivity were extremely consistent across stimulations, metrics of criticality varied across the stimulations including the deviation of criticality coefficient and shape collapse error (Fig. 8c). There were no significant differences in either metric (Fig. 8c). The branching ratio, however, showed a significant increase following stimulation (Fig. 8c), suggesting that the neural organoids are becoming more critical after stimulation.

Long-term effects of TBS on organoids were assessed by quantifying criticality, connectivity, network-level dynamics (including interspike interval, interspike interval CV, and firing rate), and spike sorted unit (aka neuronal) level changes in firing rate in wells that demonstrated input-specific STP (Supplementary Figs. 17 and 18). These metrics were quantified before and at 60 – 180 minutes post-TBS. There were no significant differences before and after stimulation (after stimulation includes grouped data from 60–180 minutes post stimulation) for all connectivity and criticality metrics (Supplementary Figs. 17 and 18). In addition, there were no consistent trends over time for network level interspike interval, interspike

interval CV, or firing rate for wells exhibiting STP (Supplementary Figs. 17 and 18). Interspike Interval (ISI) was calculated with a 4 Hz threshold (up to 250 ms) to account for changes in theta entrainment/phase locking. Well 4A, 5A, 1B, 2B, 3B, and 4B showed no long-term changes in ISI after stimulation (Supplementary Figs. 17c and 18c). While well 6A showed a significant increase in ISI 60–180 min post stimulation, apart from at 90 minutes (Supplementary Fig. 17c). The CV was used to measure ISI variability across timepoints⁷. A CV of 2.5 indicates a perfect Poisson process^{7,49}, while a CV near zero indicates a perfectly periodic spike train. All wells analyzed showed no significant change in ISI CV after stimulation (Supplementary Figs. 17c and 18c). In addition, none of the wells showed any changes in firing rate over time compared to the baseline (Supplementary Figs. 17d and 18d). Since network level ISI, ISI CV, and firing rate graphs were analyzed based on overall trends across grouped units for each well and not on a unit level, the results indicate that there are no network level changes in interspike interval or firing rate. Together, these results suggest that there are no long-term changes to the network dynamics after TBS to an individual neuron. This is expected as the TBS was input-specific; therefore, we focused on unit-level changes rather than network-level changes. Upon further investigation of unit-level firing rates over time, linear regression analysis showed that all wells had units that were either potentiated or depressed and were maintained for 180 minutes post-stimulation (Fig. 8d). To account for random changes in firing rate, the same analysis was performed on a time series recording without stimulation. In this recording, only one out of 40 units showed potentiated firing rate over time, therefore, this can be considered the noise level of changes due to basal synaptic plasticity within the organoids. Wells 4A–6A and 2B–4B show potentiated and depressed units above this level (Fig. 8d). Representative LTP and LTD units are shown in Fig. 8d. Together, these data indicate there are input-specific TBS-induced changes in connected neurons (aka units) over hours but not the overall network, supporting the use of this model to modulate input-specific short- and long-term synaptic plasticity and detect changes in synaptic plasticity in connected neurons. In addition, due to the nature of input-specific synaptic plasticity on a HD-MEA, it is difficult to control what kind of neuronal circuits are being modulated, whether they are increased or decreased, which could explain why the population of LTP compared to LTD is different in each well.

Discussion

By studying key molecular and functional changes in organoids, we aim to validate neural organoids as an *in vitro* model of learning and memory, providing a human-relevant platform for translating basic science to human applications. Despite recent studies on brain organoid electrophysiology, investigations into connectivity, criticality, and input-specific synaptic plasticity remain limited. In addition, there are no studies to our knowledge that examine immediate early gene expression following spontaneous and evoked activity in hiPSC-derived neural organoids. Our study examined spontaneous and evoked neuronal network dynamics, functional connectivity, IEG expression, and input-specific synaptic plasticity, offering insights into the molecular and cellular basis of learning and memory in bMPS systems.

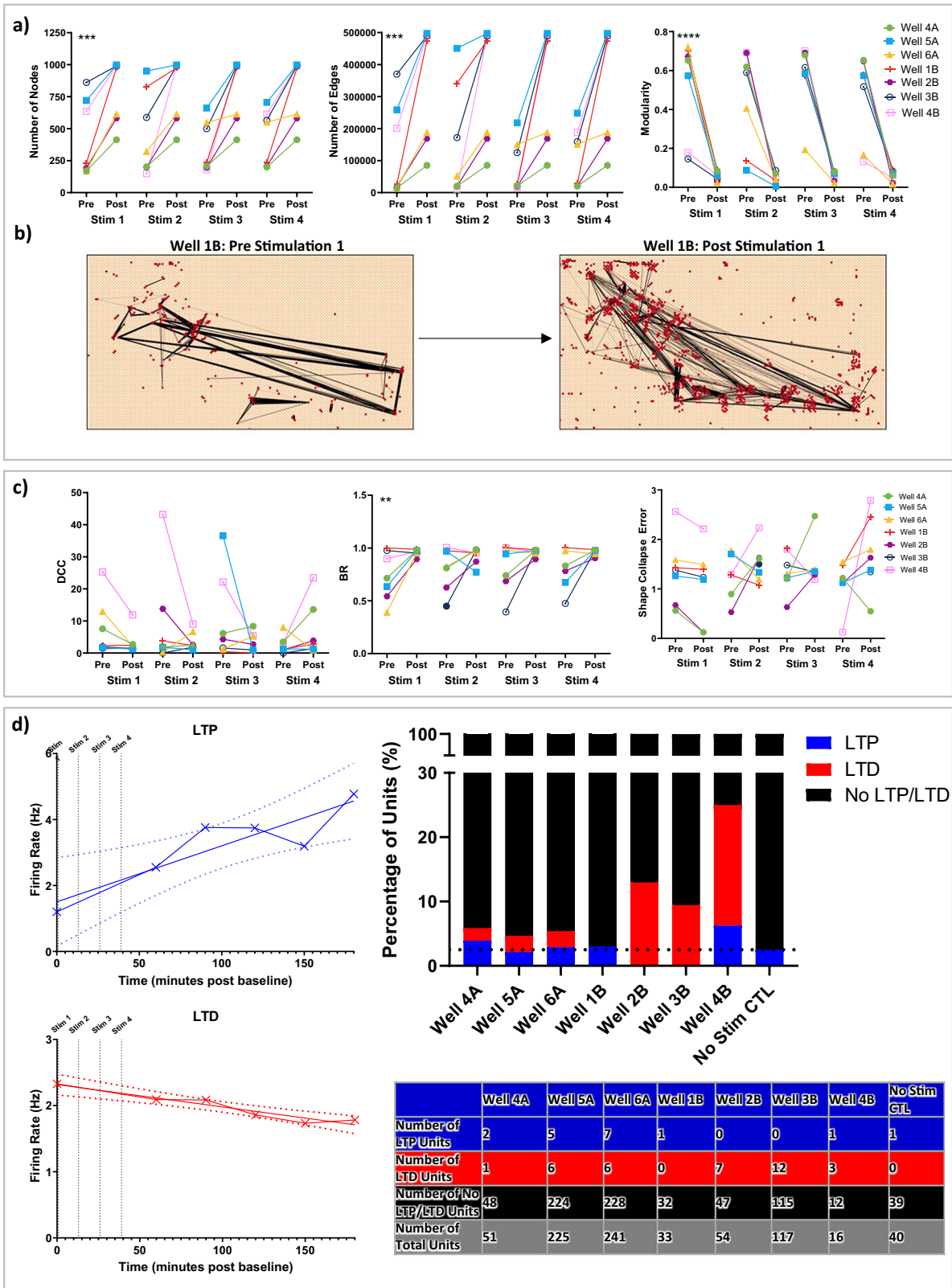


Fig. 8 | Theta-burst stimulation drives short-term changes in connectivity and criticality and long-term potentiation and depression of neuronal units.

a Connectivity metrics for all wells that demonstrated STP. **b** Representative connectivity graph before and immediately following TBS #1 for well 1B. **c** Criticality metrics for all wells that demonstrated STP. The data represents the mean of seven biological replicates from two independent experiments. A Wilcoxon matched-pairs signed rank test was performed to determine statistical significance for **a** and **c**. ** $p < 0.01$, *** $p < 0.001$, **** $p < 0.0001$. Exact p-values are listed in Supplementary Tables 22–27. For **a** and

c green circle represents well 4A, blue square – well 5A, yellow triangle – well 6A, red line – well 1B, purple circle – 2B, open blue circle – 3B, open pink square – 4B. **d**) Quantification of input-specific long-term potentiation (LTP) and depression (LTD) by measuring firing rate over time in neuronal units. Two example units demonstrating either LTP (blue line with 95% confidence intervals depicted with dashed lines) or LTD (red line, with 95% confidence intervals depicted with dashed lines) are shown on the left. The proportion of neuronal units that demonstrated LTP (red) or LTD (blue) across wells is demonstrated and quantified on the right.

IEGs are restricted to the neurons that are engaged in learning, making their expression a prerequisite of learning capabilities. We showed the expression of *ARC*, *EGR1*, *BDNF*, *NPAS4*, *NPTX2*, and *FOS* in organoids. *ARC* and *EGR1* (also known as *Zif268*, *Krox-24*, or *NGFI-A*) are calcium-regulated IEGs essential for late LTP and long-term memory^{50,51}. Additionally, *CAMK2A* is a key protein involved in synaptic plasticity and memory^{52,53}. When *CAMK2A* is activated, it phosphorylates *CREB*, allowing it to bind to the cAMP response element on the DNA⁵⁴. *CREB*, while not an IEG, is a transcription factor vital for the expression of IEGs, including *ARC* and *BDNF*^{55,56}. *CAMK2* can phosphorylate *SYNGAP1*, mediating LTP^{57–59}. Therefore, the expression of IEGs and synaptic plasticity-related genes supports the potential for LTP in the neural organoids (Fig. 2C). Synaptic and neuronal markers showed different intensity levels at 8 and 12 weeks, which might be due to the higher expression of astrocyte markers. Single-cell RNA sequencing should be conducted in future experiments to quantify precisely the different neural cell types. We also showed the expression of synaptic plasticity-related miRNAs. *miR-124-3p* controls signaling molecules involved in synaptic plasticity and memory formation, and *miR-132-3p* responds to neuronal activity in vivo and may play a role in experience-dependent neuronal plasticity^{60,61}. In contrast, *mir-134-3p* is important for synaptic downscaling⁶² and inhibition of *mir-134-3p* has been shown to rescue LTP⁶³. Confirming this, our model showed reciprocal expression of *miR-124-3p* and *miR-132-3p* with *miR-134-3p*. Using calcium imaging, organoids exhibited spontaneous bursting starting at 4 weeks of differentiation. Calcium imaging transients showed higher frequency bursting events in week 4 to 6 organoids. At week 8, calcium transients had longer burst duration, indicating sustained action potentials. These changes in calcium dynamics over time are consistent with results from dissociated rat cells cultured in 3D^{64,65}. The changes in calcium transients over time could be attributed to changes in cellular populations after 8 weeks (i.e., the differentiation of glia cells), when the largest change in calcium oscillation occurs. Specifically, we observed astrocytes with increased maturity, indicated by higher *GFAP* expression, and enhanced functionality, reflected by the elevated *AQP4* expression. Physiologically, astrocytes provide homeostatic control of neuronal activity potentially preventing hyperactivity in more mature cultures through several mechanisms, including regulation of extracellular potassium levels⁶⁶ and glutamate uptake⁶⁷. Overall, it has been demonstrated previously that the presence of astrocytes significantly modulates neuronal network activity in vitro⁶⁸. Functional inhibition of astrocytes could experimentally prove our hypothesis in future experiments. The recording of Ca^{2+} transients was technically limited to 6 min, thus the absence of the oscillation at week 12 can indicate longer interburst intervals rather than absence of the activity (activity confirmed with HD-MEA recordings).

Further HD-MEA analysis showed differing network dynamics among the different age groups. When compared to the 10-to-13 week age group, the week 6-to-9 group had higher frequency bursting events, a larger number of nodes and edges and lower number of modularity indicating a robust and connected network of neurons; showed higher neurite outgrowth as shown in active area over time (Fig. 4c) likely contributing to the lower modularity (Fig. 5d). As the organoids matured, they had fewer nodes but stronger connections, approaching a critical state and confirming system maturity. Understanding criticality in organoid models allows us to better understand the relevance and application of these models in experimental studies. Interestingly, the reduced bursting and lower network complexity in the 10-to-13 week group may also be linked to astrocytes with increased maturity in this age group, as indicated by RNA-sequencing data (Supplementary Fig. 3).

Electrical activity over time showed a high standard deviation across both groups, with a higher standard deviation in the week 10-to-13 group. A small subset of the week 10-to-13 group was never active) while the majority of week 6-to-9 organoids remained active throughout this period (Figs. 3b and 4c). This highlights the variability of organoid's HD-MEA electrophysiology data and implies that the sample size needs to be high enough to account for this variability.

Neural organoids responded as expected to pharmacological challenges with receptor agonists and antagonists, indicating functional synapse receptors and channels. 4-AP and bicuculline have been used in previous studies to induce chemical long-term potentiation (LTP) as they increase synaptic transmission⁶⁹. Therefore, stimulating with 4-AP and bicuculline, then quantifying IEG expression and neuronal network activity confirmed that organoids express the molecular machinery involved in LTP. The organoids responded electrically to bicuculline, but the bulk RNA gene expression data showed no significant increase in IEG expression after bicuculline treatment. This is likely because the population of GABAergic neurons is smaller than glutamatergic neurons in the model, making the IEG expression changes upon blockage of GABAergic neurons more difficult to detect with bulk gene expression. It has been estimated that the ratio of GABAergic neurons to other neurons in cortical regions is 1 to 5 or 20 percent^{70,71} therefore our small population of GABAergic neurons corresponds with these estimations.

NPAS4 gene expression is induced by calcium influx in the post-synaptic terminal after neuronal activity⁷², this correlates with our findings that 4-AP exposure caused an increase in *NPAS4* expression in both week 8 and 13 organoids. Interestingly, *NPAS4* regulates the expression of multiple genes including *BDNF* and *NPTX2*⁷². While we detected an increase in *NPAS4* gene expression, we did not observe an increase in its downstream targets *BDNF* and *NPTX2*. This can be explained by the time point of sample collection (2 hours after exposure), and an increase in the downstream targets might be seen later. NBQX and AP5 disrupt excitatory glutamatergic synaptic transmission, specifically network bursting, therefore, as expected there is no change in expression of synaptic plasticity-related genes after the addition of these compounds.

After electrical theta burst stimulation, neuronal synaptic plasticity, connectivity, and criticality were investigated. We identified candidate neuronal units from spike sorting that showed an increase in activity immediately after stimulation and were maintained for short time periods. This approach towards teasing apart input-specific synaptic plasticity on HD-MEAs by identifying one neuron to stimulate (using 32 electrodes) and quantifying the effects of stimulation among neuronal units, allows for the determination of input-specific synaptic plasticity rather than network-level events that previous MEA-based studies have investigated. Longer time scale analysis indicated neuronal units across wells maintained increased or decreased firing rates for up to 180 minutes following stimulation, demonstrating the TBS could have input-specific long-term effects on sub populations of neurons within organoids. In addition, criticality changed after TBS and drove the organoids to a more critical state. Despite this, critical dynamics after the TBS were not as pronounced as previously reported when neuronal systems are exposed to more structured stimulation in a closed-loop setup³⁰. This supports the theory that neuronal criticality arises in dynamic systems when presented with structured information, maximizing information capacity and transmission through the network. Here, less structure was contained in the signal presented to the cultures compared with previous work³⁰, and therefore while there was a shift towards a more critical state, a greater shift might be observed if the signal contained greater complexity. These results highlight the value of considering criticality as a continuum. The ability to see nuanced changes supports using criticality as an endpoint to assess synaptic plasticity. The lower baseline activity in wells 1A-3A resulted in a relatively low number of active neurons after spike sorting and low connectivity (Supplementary Fig. 10b), which could explain the absence of response after stimulation in these wells. Thus, a certain baseline activity threshold should be set up and used as acceptance/validity criteria for such experiments to increase reproducibility.

Our results are consistent with previously published studies showing that neural organoids can exhibit synaptic plasticity^{14,33,35,36} and that stimulation can drive changes in connectivity¹⁴. In monolayers, nuanced changes in functional connectivity have even been associated with learning effects⁷³. Yet while, recent studies demonstrated short^{14,33,35,36} and long-term synaptic plasticity in neuronal organoids^{35,36}, these studies either used traditional patch clamp methods³⁵ or assessed network dynamics on low

density MEAs rather than traditional LTP³⁶. Based on our review, input-specific short- and long-term potentiation/depression in neural organoids using HD-MEAs has not been shown yet. No previous studies have investigated how input-specific short- and long-term synaptic plasticity impacts criticality in neural organoids. In addition, to the best of our knowledge, this is the first demonstration of evoked IEG expression upon chemical LTP induction. Further research using more complex models is needed. Cortical-hippocampal assembloids would be essential to study the mechanisms of learning and memory, as specific synapses in the hippocampus are pivotal for these functions^{74–76}. Recent advances, such as the development of a human ascending somatosensory assembloid that functionally integrates somatosensory, spinal, thalamic, and cortical organoids, highlight the feasibility of assembling human circuits in vitro⁷⁷. These models not only enable mechanistic studies of neural processes but also provide the foundation for exploring circuit-level plasticity relevant to cognition and disease.

Combining these functional endpoints with established disease models in organoids will enhance research on disease pathophysiology, drug development, toxicant identification and various genetic, infectious, neurodevelopmental, and neurodegenerative disorders^{32,78}.

This study builds on the concept of OI¹³ by exploring the molecular and functional aspects of synaptic plasticity underlying learning and memory capabilities in neural organoids. An OI community is forming, which is embracing the ethical challenges of this approach^{79,80}. As more advanced methods of generating data from these models attracts further multidisciplinary interest in this work⁸¹, more advanced machine learning methods, such as reinforcement learning in the bMPS model and in more complex bMPS models will be explored, advancing the concept of “learning-on-chip” towards OI. Ultimately, here we provide compelling evidence for the utility of these organoid models not just for studying neurophysiological function and development, but as ones that may serve as a tool for even more advanced applications in the future.

Methods

Brain Microphysiological System

Female fibroblast (donor cell material: MRC-9)-derived NIBSC8 (N8) iPSCs were obtained from the National Institute for Biological Standards and Control, NIBSC (NIBSC), UK with a certificate of analysis identifying that they have no mycoplasma, bacteria, or viruses and have normal karyotype as identified by SNP Array. hiPSCs were cultured in mTESR-Plus medium (StemCell Technologies) at 5% O₂, 5% CO₂ and 37 °C. Stemness was confirmed with Oct4, Nanog, TRA-1-61, and Sox2 by immunocytochemistry and flow cytometry¹¹. hiPSCs cells were then differentiated in a monolayer to neuroprogenitor cells (NPCs) using a serum-free, neural induction medium (Gibco, Thermo Fisher Scientific). Nestin/Sox2-positive NPCs were then expanded and seeded in uncoated 6-well plates using a neural expansion medium: 24.5 mL neurobasal media (Thermo Fisher Scientific), 24.5 mL advanced DMEM/F12 (Thermo Fisher Scientific), and 1 mL neural induction supplement (Thermo Fisher Scientific). Expanded NPCs were then dissociated into a single cell suspension and 2 million cells were seeded into each well of a 6-well plate and placed on a shaker. These cultures were kept at 37 °C, 5% CO₂, and 20% O₂ under constant gyratory shaking (88 rpm, 19 mm orbit) to form spheres. Due to the gyratory shaking in uncoated plates, the cells self-organized and aggregated in spherical shape. After 48 hours, differentiation was induced by replacing the medium with neural differentiation medium: B-27[™] plus kit, 1% Glutamax (Gibco, Thermo Fisher Scientific), 10 ng/ml human recombinant GDNF (GeminiBio[™]), 10 ng/ml human recombinant BDNF (GeminiBio[™]), 1% Pen/Strep/Glutamine (Gibco, Thermo Fisher Scientific). Half changes of medium were performed 3 times a week. The cultures were kept under constant gyratory shaking for up to 14 weeks, which allowed unguided differentiation and maturation of different types of neurons, astrocytes and oligodendrocytes, promoting synaptogenesis and tight intercellular interactions. Organoid age was counted starting from the day the cells are placed on the gyratory shaker to form 3D cultures.

Immunocytochemistry

Immunocytochemistry was performed as described in Romero et al.¹¹. After fixation in 2% PFA, organoids were permeabilized with 0.1% Triton X and blocked with 100% BlockAid[™]. After blocking, cultures were stained with primary antibodies (Supplementary Table 1) at 4 °C on a shaker for 24 hours followed by staining with secondary antibodies for another 24 hours. Nuclei were counterstained with Hoechst 33342 trihydrochloride (Invitrogen Molecular Probes) at a concentration of 1:10,000. No primary antibody controls were used as negative controls. Images were taken with a FV3000RS Olympus confocal microscope. Further imaging processing and quantification were performed using ImageJ2.

RT-qPCR

Total RNA (including small non-coding RNA) was isolated via a Quick-RNA[™] Microprep Kit (Zymo Research). The NanoDrop[™] 2000c Spectrophotometer (Thermo Fisher Scientific) was used to determine RNA quality and quantity. mRNA reverse-transcription was performed using M-MLV Reverse Transcriptase and Random Hexamer primers (Promega) according to the manufacturer’s instructions. The expression of genes was evaluated using both SYBR Green (Thermo Fisher Scientific) and TaqMan gene expression assay (Applied Biosystems) on a 7500 Fast Real-Time system (Supplementary Tables 2 and 3). Actin beta (*ACTB*) and *18S* were used as reference genes for SYBR Green and TaqMan, respectively. For microRNA, conversion to cDNA was performed according to the QIAGEN miRCURY LNA RT Kit Quick-Start Protocol. Small nucleolar RNA C/D box 44 (*SNORD44*) was used as a reference gene. An overview of the SYBR[®] Green primers designed and the TaqMan and miRCURY LNA primers used for this study can be seen in Supplementary Tables 2 and 3.

Pharmacological neurotransmission modulation

Two age groups (8 weeks and 13 weeks +/-4 days) of organoids were treated with 20 μM 2,3-dioxo-6-nitro-7-sulfamoyl-benzo[f]quinoxaline (NBQX), 20 μM D-2-amino-5-phosphonovalerate (AP5), 100 μM 4-Aminopyridine (4-AP), or 10 μM bicuculline for 2 hours in 6-well plates. 30–40 organoids per replicate were collected after 2 hours, washed 2 times with PBS, and then snap frozen for later RNA extraction. Synaptic plasticity-related gene expression was measured 2 hours after exposure to pharmacological agents and compared to the corresponding untreated 2 hour control in the two age groups. In addition, 13-week-old organoids that had been plated on high-density MEAs for 29 days were also stimulated with 20 μM NBQX, 20 μM AP5, 100 μM 4-AP, or 10 μM bicuculline for 2 hours. Electrical activity was recorded before (baseline), immediately after (time 0), as well as 2 and 4 hours after the addition of the pharmacological agents.

To elucidate the remaining spiking activity, 40 μM NBQX, 40 μM AP5, 10 μM bicuculline, 10 μM CPG 55845, 5 μM 6-OHDA, 10 μM haloperidol, and 1 nM CPF-Oxone were used in various combinations to modulate different cell types.

Calcium imaging

Organoids were incubated with 10 μM Fluo-4AM (Tocris) and 0.5% Pluronic Acid (Invitrogen) in the dark for 2 hours at 37 °C and 5% CO₂ without shaking. After 3 washing steps, organoids were transferred to a glass-bottomed 24-well plate to be imaged with the resonant scanner in an Olympus FV3000-RS with a speed of 12.5 frames per second for 6 minutes. They were kept at 37 °C and 5% CO₂ throughout imaging. Raw fluorescent intensities of the whole organoid over time were processed using the ROI manager in ImageJ and further analyzed using a custom python script to obtain ΔF/F plots (https://github.com/organoid-intelligence/bMPS_analysis_tools).

High-Density Microelectrode Array (HD-MEA)

MaxWell Biosystems 6-well HD-MEA chips were coated for 1 hour at 37 °C and 5% CO₂ with 0.07% Poly(ethyleneimine) solution (Sigma Aldrich) diluted in 1x borate buffer (Thermo Fisher Scientific). Chips were then

washed 3 times with water and dried in a sterile hood for 1 hour. 0.04 mg/ml mouse Laminin (Sigma Aldrich) was diluted in neural differentiation medium and placed on the chips for 1 hour incubation at 37 °C and 5% CO₂. The laminin was then removed and organoids were placed on the MEA in neural differentiation medium. Two different age groups were plated on the HD-MEA: 5.5- and 9.5 week old organoids. Activity was measured every other day starting at day 3 to 21 on the MEA. The day organoids were put on the chip was considered DOM 0 (Day on MEA). The MaxWell Biosystems MaxLab-live Software (version 22.2.6, Switzerland) was used to calculate percent active area, interspike interval within burst, burst interspike interval, interburst interval coefficient of variation, burst peak firing rate, spikes per burst per electrode, spikes per burst, spikes within bursts, burst frequency, burst duration, interspike interval outside bursts. A gain of 512x, high-pass filter of 300 Hz and spike threshold of 5.5 RMS mV were used during all recordings.

Theta Burst Stimulation Protocol

The Theta Burst Stimulation (TBS) protocol utilized 4 sets of pulse trains delivered with a phase of 100 μs, amplitude of 800 mV, and a time between pulses of 10.2 ms. 10 sequences of these 4 pulse trains were delivered and considered one TBS. Four spaced TBS (13-minute interval between TBS) were delivered to induce a persistent potentiation. Individual neuronal footprints for each well were identified based on spike sorting using the MaxLab-live Axon Tracking Assay. One neuronal footprint within each well was randomly chosen and TBS was administered to 32 electrodes per well (Supplementary Fig. 12 and 13). Therefore, one neuron in each well was chosen to be stimulated using 32 electrodes. To investigate the receptors contributing to potentiated electrode response, one well was treated with NBXQ/AP5 prior to being stimulated with the TBS protocol. Two independent experiments (referred to as A and B) were conducted. Wells 1 A through 6 A were tested in experiment A and Experiment B included Wells 1B through 4B.

Bulk RNAseq sample preparation

N8 organoids differentiated for 8, 12, or 13 weeks were washed with ice-cold PBS and flash frozen. Six replicates were processed for week 8 samples, three - for week 12, and four - for week 13. Total RNA was isolated using the Quick-RNA™ Microprep Kit (Zymo Research). The integrity of the RNA was verified on the Agilent TapeStation 4200 (Agilent technologies). 500 ng of total RNA were used to prepare mRNA libraries with the TruSeq Stranded mRNA Library Prep Kit (Illumina) according to the manufacturer's protocol. This process included the purification of Poly-A containing mRNA, fragmentation of mRNA, first- and second-strand cDNA synthesis, adenylation of 3' ends, and ligation of TruSeq RNA Combinatorial Dual Indexes (Illumina). Ligated fragments were amplified for 15 cycles, purified, and quantified using the Qubit 3.0 Fluorometer (Thermo Fisher Scientific). The size distribution and quality of the libraries were assessed using the Agilent TapeStation 4200. The libraries were normalized, pooled, and sequenced on the NovaSeq X Plus (Illumina) with 150 bp paired-end reads, achieving a coverage of about 100 million reads per sample.

Bulk-RNA Sequencing Analysis

bRaw FASTQ files were processed using the nf-core rna-seq pipeline, which leverages Nextflow workflows (version 23.10.1)^{82,83}. Adapters and poor-quality sequences were trimmed using "Trim-Galore!"⁸⁴. Reads were aligned to the GRCh38 genome using ENSEMBL gene annotations (release 111) using STAR, and transcripts were quantified with Salmon⁸⁵⁻⁸⁷. Post processing of reads was accomplished using SAMtools (sorting and indexing alignments), picard (duplicate identification), and BEDtools (genome coverage assessment)⁸⁸⁻⁹⁰. Read and mapping quality were assessed using RSeQC, Qualimap, dupRad, and Preseq⁹¹⁻⁹⁴. Outliers were assessed using DESeq2 PCA plots⁹⁵. A list of regional and lineage-specific marker genes was obtained from Human Protein Atlas and previous publications⁷. Gene expression data were normalized using the weighted trimmed mean of the log expression ratios (TMM) using the R package tidybulk and log2-

transformed⁹⁶. The comprehensive gene list for Supplementary Figs 2, 3, 4 and 6 are included in supplementary data 4.

Functional connectivity analysis

First, we grouped the spiking data into bins of spikes, with a set length. In this study, we used a window of 100 ms, with a 50 ms sliding window to sort spikes into bins. Each bin captures n number of spikes.

Binning was performed as a pre-requisite for the mutual-information calculation, which requires probabilities (log₂) of spiking or not spiking.

Mutual information was calculated according to Eq. (1).

$$I(X, Y) = H(X) + H(Y) - H(X, Y) \quad (1)$$

where X and Y are two unique electrodes (nodes), H(X) and H(Y) are the marginal entropies (Eq. 2) and H(X,Y) is the joint entropy of X and Y (Eq. 3)⁹⁷.

Here, marginal entropy was calculated as using the Shannon entropy formula; Eq. (2).

$$H(X) = - \sum_{x \in X} p(x, y) \log_2 p(x) \quad (2)$$

where p(x) is a probability mass function of spikes occurring in either electrode X or electrode Y across windows. Log₂ was used to reflect a binary choice (spike vs non-spike).

Joint entropy was also calculated using the Shannon entropy formula; Eq. (3).

$$H(X, Y) = - \sum_{x \in X} \sum_{y \in Y} p(x, y) \log_2 p(x, y) \quad (3)$$

where p(x,y) is the joint probability of X and Y spiking together.

A distance matrix was constructed from the mutual information across all bins. The distance matrix reflects the probability of each electrode spiking or not spiking, in relation to each other electrode, across the entire time series. Graphically, electrodes were treated as nodes, and mutual information between electrodes was designated as an edge. The width of the edge between electrode X and Y reflects the mutual information score (between 0 and 1), where 1 is a high probability of electrode X spiking at the same time electrode Y spikes, and 0 is a low probability of this occurring.

Since distance matrices were constructed from spiking data, binning across time windows was required to generate probabilities of firing or not firing for each electrode (e.g., in bin 1, electrodes 2 and 3 might fire together, but in bin 2, they might not, therefore, the probability of them firing together across those bins is 0.5).

Graphical representations of distance matrices were overlaid on x, y positions of all electrodes used in the recording to generate a map of average electrode activity across recordings. Electrodes with at least one spike in any bin are highlighted in red. Only the 200 strongest edges are shown for clarity of visualization. The edge strengths were exponentially scaled to make it easier to visualize on a single plot.

Criticality analysis

Criticality was quantified by calculating the deviation from criticality coefficient (DCC), branching ratio (BR), and shape collapse error (SCe). Criticality implies that the system is defined by scale-free dynamics and that events in both the spatial and temporal domains obey power laws. Here, these events are contiguous cascades of spiking activity, rather than limited local bursts of spiking activity or huge network-wide spiking events. These contiguous cascades of spiking activity are called neuronal avalanches. Now, each power law distribution fitted to avalanche size (number of contributing spikes to an avalanche) and avalanche durations can be represented by a coefficient which we call τ and α , respectively. Now, in critical systems, there is another exponent relationship between mean avalanche sizes ($\langle S \rangle$), given

their duration, D as Eq. (4).

$$\langle S \rangle \propto D^{\alpha} (\beta_{fit}) \quad (4)$$

This β_{fit} is derived from the experimental data using linear regression. This third power law exponent also relates the size and duration distributions of the avalanches above and is predicted mathematically by Eq. (5).

$$\beta_{pred} = (\alpha - 1) / (\tau - 1) \quad (5)$$

Now, comparing the fitted value from the empirical data (β_{fit}) and its estimation using α and τ exponents (β_{pred}), a new measure is derived to evaluate the Deviation from Criticality Coefficient (DCC), parameterized as dCC ; Eq. (6).

$$dCC = ||\beta_{pred} - \beta_{fit}|| \quad (6)$$

Consequently, a smaller DCC value indicates a more accurate fit power law distribution to the empirical data and a system that is closer to criticality.

In addition, the branching ratio (BR) is defined as the ratio of the number of units (neurons) active (spiking) at time step $t + 1$ to the number of active units (neurons) at time step t . Since a critical regime is naturally balanced and avoids runaway gains, the critical branching ratio is 1.

Finally, another feature of critical dynamics is that avalanche shapes show fractal properties, and all avalanche profiles of different sizes are scaled versions of the same universal shape. The result of shape collapse error (SCe) basically measures how accurately avalanches of all different durations can be scaled (collapsed) to the same universal shape.

Spike sorting

Spike sorting was performed through a custom Python pipeline using Kilosort2⁹⁸ and Spikeinterface⁹⁹. First the raw extracellular recordings were band-pass filtered between 300–6000 Hz. The filtered traces were then spikesorted using the Kilosort2 algorithm. Finally, the results were further curated by removing units with more than 1% of interspike intervals smaller than 1.5 ms, an average firing rate below 0.05 Hz and/or a signal-to-noise ratio below 5.

Statistics and reproducibility

All graphs and statistical analysis were done in GraphPad Prism, version 9.5.1. Not significant (ns) $p > 0.05$; $*p < 0.05$; $**p < 0.01$; $***p < 0.001$; $****p < 0.0001$. Throughout the text, independent experiments refer to the different differentiation batches, while technical replicates refer to the different wells with organoids within one independent experiment.

Statistical changes in calcium transient dynamics over time (Fig. 3) were analyzed with one-way ANOVA with Tukey post hoc test. At least 8 individual organoids across at least 3 independent experiments were imaged and quantified for each time point.

Changes in network activity from HD-MEA recordings over time were calculated using a mixed-effects model with matching and a Tukey post-hoc test (Fig. 4). Changes in criticality and connectivity over time were calculated using a two-way ANOVA and a Tukey post-hoc test (Fig. 5). For these HD-MEA time-course experiments, data were collected from two independent experiments, each including 5–6 HD-MEA wells per group, with 2–5 organoids per well.

mRNA gene expression changes after stimulation with pharmacological agents were analyzed with a one-way ANOVA with Dunnett's post-hoc tests (Fig. 6 and Supplementary Fig. 8). Data for this experiment came from 3 independent experiments with 2 technical replicates each for 8-weeks and 4–5 independent experiments with 2 technical replicates each for 13-week time point.

Network activity changes after stimulation with pharmacological agents were analyzed with a repeated measures ANOVA with Tukey post-hoc tests (Fig. 6). This experimental data came from 3 independent experiments with 2 HD-MEA wells per experiment per chemical.

Network connectivity and criticality changes before and after stimulation were determined with a two-tailed paired t-test (Supplementary Figs. 17 and 18). Network-level ISI, ISI CV, and firing rate were first processed to identify and exclude outliers using the ROUT method ($Q = 1\%$), followed by statistical analysis using a one-way ANOVA and Dunnett's post-hoc tests (Supplementary Figs. 17 and 18). Short-term network level changes in criticality and connectivity were determined with a Wilcoxon matched-pairs signed rank test (Fig. 8). Unit-level long-term potentiation was quantified using a linear regression of firing rate over time. These data came from two independent experiments with 4–6 wells per experiment, with 4–5 organoids per well.

Reporting summary

Further information on research design is available in the Nature Portfolio Reporting Summary linked to this article.

Data availability

All source data underlying the graphs and charts presented in the main figures are included in Supplementary Data 1 and 2. RNA-seq data from the organoid samples are deposited in the NCBI Gene Expression Omnibus <https://www.ncbi.nlm.nih.gov/geo/query/acc.cgi?acc=GSE301725>. Any additional information required to reanalyze the data reported in this paper is available from the lead contact upon request.

Code availability

The calcium imaging, and network connectivity and criticality code has been deposited at https://github.com/organoid-intelligence/bMPS_analysis_tools and is publicly available.

Received: 23 September 2024; Accepted: 30 July 2025;

Published online: 16 August 2025

References

- Smirnova, L. & Hartung, T. The promise and potential of brain organoids. *Adv. Healthc. Mater.* e2302745 <https://doi.org/10.1002/adhm.202302745> (2024).
- Acharya, P., Choi, N. Y., Shrestha, S., Jeong, S. & Lee, M.-Y. Brain organoids: A revolutionary tool for modeling neurological disorders and development of therapeutics. *Biotechnol. Bioeng.* **121**, 489–506 (2024).
- Birey, F. et al. Assembly of functionally integrated human forebrain spheroids. *Nature* **545**, 54–59 (2017).
- Qian, X. et al. Brain region-specific organoids using mini-bioreactors for modeling ZIKV exposure. *Cell* **165**, 1238–1254 (2016).
- Quadrato, G. et al. Cell diversity and network dynamics in photosensitive human brain organoids. *Nature* **545**, 48–53 (2017).
- Sloan, S. A. et al. Human astrocyte maturation captured in 3D cerebral cortical spheroids derived from pluripotent stem cells. *Neuron* **95**, 779–790.e6 (2017).
- Sharf, T. et al. Functional neuronal circuitry and oscillatory dynamics in human brain organoids. *Nat. Commun.* **13**, 4403 (2022).
- Paşca, A. M. et al. Functional cortical neurons and astrocytes from human pluripotent stem cells in 3D culture. *Nat. Methods* **12**, 671–678 (2015).
- Kagan, B. J. et al. The technology, opportunities, and challenges of Synthetic Biological Intelligence. *Biotechnol. Adv.* **68**, 108233 (2023).
- Pamies, D. et al. A human brain microphysiological system derived from induced pluripotent stem cells to study neurological diseases and toxicity. *ALTEX* **34**, 362–376 (2017).
- Romero, J. C. et al. Oligodendrogenesis and myelination tracing in a CRISPR/Cas9-engineered brain microphysiological system. *Front Cell Neurosci.* **16**, 1094291 (2022).
- Trujillo, C. A. et al. Complex oscillatory waves emerging from cortical organoids model early human brain network development. *Cell Stem Cell* **25**, 558–569.e7 (2019).

13. Smirnova, L. et al. Organoid intelligence (OI): the new frontier in biocomputing and intelligence-in-a-dish. *Front. Sci.* **1**, 1017235 (2023).
14. Cai, H. et al. Brain organoid reservoir computing for artificial intelligence. *Nat. Electron.* **6**, 1032–1039 (2023).
15. Robbins, A. et al. Goal-Directed Learning in Cortical Organoids. *BioRxiv Prepr. Serv. Biol.* 2024.12.07.627350 <https://doi.org/10.1101/2024.12.07.627350> (2024).
16. Citri, A. & Malenka, R. C. Synaptic Plasticity: Multiple Forms, Functions, and Mechanisms. *Neuropsychopharmacology* **33**, 18–41 (2008).
17. Kotaleski, J. H. & Blackwell, K. T. Computational Neuroscience: Modeling the Systems Biology of Synaptic Plasticity. *Nat. Rev. Neurosci.* **11**, 239–251 (2010).
18. Mateos-Aparicio, P. & Rodríguez-Moreno, A. The Impact of Studying Brain Plasticity. *Front. Cell. Neurosci.* **13**, 66 (2019).
19. Stampanoni Bassi, M., Iezzi, E., Gilio, L., Centonze, D. & Buttari, F. Synaptic Plasticity Shapes Brain Connectivity: Implications for Network Topology. *Int. J. Mol. Sci.* **20**, 6193 (2019).
20. Bliss, T. V. P. & Lomo, T. Long-lasting potentiation of synaptic transmission in the dentate area of the anaesthetized rabbit following stimulation of the perforant path. *J. Physiol.* **232**, 331–356 (1973).
21. Morris, R. G., Anderson, E., Lynch, G. S. & Baudry, M. Selective impairment of learning and blockade of long-term potentiation by an N-methyl-D-aspartate receptor antagonist, AP5. *Nature* **319**, 774–776 (1986).
22. Volianskis, A., Collingridge, G. L. & Jensen, M. S. The roles of STP and LTP in synaptic encoding. *PeerJ* **1**, e3 (2013).
23. Volianskis, A. & Jensen, M. S. Transient and sustained types of long-term potentiation in the CA1 area of the rat hippocampus. *J. Physiol.* **550**, 459–492 (2003).
24. France, G. et al. Differential regulation of STP, LTP and LTD by structurally diverse NMDA receptor subunit-specific positive allosteric modulators. *Neuropharmacology* **202**, 108840 (2022).
25. Davies, S. N., Lester, R. A., Reymann, K. G. & Collingridge, G. L. Temporally distinct pre- and post-synaptic mechanisms maintain long-term potentiation. *Nature* **338**, 500–503 (1989).
26. Anwyl, R., Mulkeen, D. & Rowan, M. J. The role of N-methyl-D-aspartate receptors in the generation of short-term potentiation in the rat hippocampus. *Brain Res.* **503**, 148–151 (1989).
27. Minatohara, K., Akiyoshi, M. & Okuno, H. Role of Immediate-Early Genes in Synaptic Plasticity and Neuronal Ensembles Underlying the Memory Trace. *Front. Mol. Neurosci.* **8**, 78 (2016).
28. Chu, H.-Y. Synaptic and cellular plasticity in Parkinson's disease. *Acta Pharmacol. Sin.* **41**, 447–452 (2020).
29. Heiney, K. et al. Criticality, Connectivity, and Neural Disorder: A Multifaceted Approach to Neural Computation. *Front. Comput. Neurosci.* **15**, 611183 (2021).
30. Habibollahi, F., Kagan, B. J., Burkitt, A. N. & French, C. Critical dynamics arise during structured information presentation within embodied in vitro neuronal networks. *Nat. Commun.* **14**, 5287 (2023).
31. Skilling, Q. M., Ognjanovski, N., Aton, S. J. & Zochowski, M. Critical Dynamics Mediate Learning of New Distributed Memory Representations in Neuronal Networks. *Entropy* **21**, 1043 (2019).
32. Watmuff, B. et al. Drug treatment alters performance in a neural microphysiological system of information processing. *Commun. Biol.* **8**, 916 (2025).
33. Osaki, T. et al. Complex activity and short-term plasticity of human cerebral organoids reciprocally connected with axons. *Nat. Commun.* **15**, 2945 (2024).
34. Molen, T. van der et al. Protosequences in brain organoids model intrinsic brain states. 2023.12.29.573646 Preprint at <https://doi.org/10.1101/2023.12.29.573646> (2025).
35. Patton, M. H. et al. Synaptic plasticity in human thalamocortical assembloids. *Cell Rep.* **43**, 114503 (2024).
36. Zafeiriou, M.-P. et al. Developmental GABA polarity switch and neuronal plasticity in Bioengineered Neuronal Organoids. *Nat. Commun.* **11**, 3791 (2020).
37. Kim, S., Kim, H. & Um, J. W. Synapse development organized by neuronal activity-regulated immediate-early genes. *Exp. Mol. Med.* **50**, 1–7 (2018).
38. Hunt, D. L. & Castillo, P. E. Synaptic plasticity of NMDA receptors: mechanisms and functional implications. *Curr. Opin. Neurobiol.* **22**, 496–508 (2012).
39. Hayashi, Y. et al. Driving AMPA receptors into synapses by LTP and CaMKII: requirement for GluR1 and PDZ domain interaction. *Science* **287**, 2262–2267 (2000).
40. Bar-Shira, O., Maor, R. & Chechik, G. Gene expression switching of receptor subunits in human brain development. *PLOS Comput. Biol.* **11**, e1004559 (2015).
41. Jeyabalan, N. & Clement, J. P. SYNGAP1: Mind the Gap. *Front. Cell. Neurosci.* **10**, 32 (2016).
42. Hu, Z. & Li, Z. miRNAs in Synapse development and synaptic plasticity. *Curr. Opin. Neurobiol.* **45**, 24–31 (2017).
43. Cocchi, L., Gollo, L. L., Zalesky, A. & Breakspear, M. Criticality in the brain: A synthesis of neurobiology, models and cognition. *Prog. Neurobiol.* **158**, 132–152 (2017).
44. Ahtiaainen, A. et al. Ketamine reduces electrophysiological network activity in cortical neuron cultures already at sub-micromolar concentrations – Impact on TrkB-ERK1/2 signaling. *Neuropharmacology* **229**, 109481 (2023).
45. Uchida, T. et al. Xenon-induced inhibition of synchronized bursts in a rat cortical neuronal network. *Neuroscience* **214**, 149–158 (2012).
46. Kelleher, R. J., Govindarajan, A. & Tonegawa, S. Translational Regulatory Mechanisms in Persistent Forms of Synaptic Plasticity. *Neuron* **44**, 59–73 (2004).
47. Nguyen, P. V. & Kandel, E. R. Brief theta-burst stimulation induces a transcription-dependent late phase of LTP requiring cAMP in area CA1 of the mouse hippocampus. *Learn. Mem.* **4**, 230–243 (1997).
48. Caneu, J. et al. A human induced pluripotent stem cell-derived cortical neuron human-on-a chip system to study Aβ42 and tau-induced pathophysiological effects on long-term potentiation. *Alzheimers Dement. Transl. Res. Clin. Interv.* **6**, e12029 (2020).
49. Poisson Model of Spike Generation | Request PDF. https://www.researchgate.net/publication/2807507_Poisson_Model_of_Spike_Generation.
50. Guzowski, J. F. et al. Inhibition of activity-dependent Arc protein expression in the rat hippocampus impairs the maintenance of long-term potentiation and the consolidation of long-term memory. *J. Neurosci.* **20**, 3993–4001 (2000).
51. Thiel, G., Mayer, S. I., Müller, I., Stefano, L. & Rössler, O. G. Egr-1—A Ca²⁺-regulated transcription factor. *Cell Calcium* **47**, 397–403 (2010).
52. Takemoto-Kimura, S. et al. Calmodulin kinases: essential regulators in health and disease. *J. Neurochem.* **141**, 808–818 (2017).
53. Zalcman, G., Federman, N. & Romano, A. CaMKII Isoforms in Learning and Memory: Localization and Function. *Front. Mol. Neurosci.* **11**, 445 (2018).
54. Kasahara, J., Fukunaga, K. & Miyamoto, E. Activation of calcium/calmodulin-dependent protein kinase IV in long term potentiation in the rat hippocampal CA1 region. *J. Biol. Chem.* **276**, 24044–24050 (2001).
55. Kim, J. & Kaang, B.-K. Cyclic AMP response element-binding protein (CREB) transcription factor in astrocytic synaptic communication. *Front. Synaptic Neurosci.* **14**, 1059918 (2023).
56. Ying, S.-W. et al. Brain-derived neurotrophic factor induces long-term potentiation in intact adult hippocampus: requirement for ERK activation coupled to CREB and upregulation of Arc synthesis. *J. Neurosci. J. Soc. Neurosci.* **22**, 1532–1540 (2002).

57. Fu, Z. et al. Differential roles of Rap1 and Rap2 small GTPases in neurite retraction and synapse elimination in hippocampal spiny neurons. *J. Neurochem.* **100**, 118–131 (2007).
58. Meili, F. et al. Multi-parametric analysis of 57 SYNGAP1 variants reveal impacts on GTPase signaling, localization, and protein stability. *Am. J. Hum. Genet.* **108**, 148–162 (2021).
59. Zhu, J. J., Qin, Y., Zhao, M., Van Aelst, L. & Malinow, R. Ras and Rap control AMPA receptor trafficking during synaptic plasticity. *Cell* **110**, 443–455 (2002).
60. Fischbach, S. J. & Carew, T. J. MicroRNAs in memory processing. *Neuron* **63**, 714–716 (2009).
61. Nudelman, A. S. et al. Neuronal activity rapidly induces transcription of the CREB-regulated microRNA-132, in vivo. *Hippocampus* **20**, 492 (2010).
62. Fiore, R. et al. MiR-134-dependent regulation of Pumilio-2 is necessary for homeostatic synaptic depression. *EMBO J.* **33**, 2231–2246 (2014).
63. Baby, N., Alagappan, N., Dheen, S. T. & Sajikumar, S. MicroRNA-134-5p inhibition rescues long-term plasticity and synaptic tagging/capture in an A β (1–42)-induced model of Alzheimer's disease. *Aging Cell* **19**, e13046 (2020).
64. Ming, Y., Hasan, M. F., Tatic-Lucic, S. & Berdichevsky, Y. Micro Three-Dimensional Neuronal Cultures Generate Developing Cortex-Like Activity Patterns. *Front. Neurosci.* **14**, 563905 (2020).
65. Marom, A., Shor, E., Levenberg, S. & Shoham, S. Spontaneous Activity Characteristics of 3D "Optonets". *Front. Neurosci.* **10**, 602 (2017).
66. Walz, W. Role of astrocytes in the clearance of excess extracellular potassium. *Neurochem. Int.* **36**, 291–300 (2000).
67. Sulkowski, G., Dąbrowska-Bouta, B., Salińska, E. & Strużyńska, L. Modulation of glutamate transport and receptor binding by glutamate receptor antagonists in EAE rat brain. *PLoS One* **9**, e113954 (2014).
68. Räsänen, N. et al. Astrocytes regulate neuronal network burst frequency through NMDA receptors in a species- and donor-specific manner. *Biol. Psychiatry Glob. Open Sci.* **4**, 100313 (2024).
69. Jiang, Y. & VanDongen, A. M. J. Selective increase of correlated activity in Arc-positive neurons after chemically induced long-term potentiation in cultured hippocampal neurons. *eNeuro* **8**, ENEURO.0540-20.2021 (2021).
70. Hendry, S. H., Schwark, H. D., Jones, E. G. & Yan, J. Numbers and proportions of GABA-immunoreactive neurons in different areas of monkey cerebral cortex. *J. Neurosci. J. Soc. Neurosci.* **7**, 1503–1519 (1987).
71. Sahara, S., Yanagawa, Y., O'Leary, D. D. M. & Stevens, C. F. The fraction of cortical GABAergic neurons is constant from near the start of cortical neurogenesis to adulthood. *J. Neurosci. J. Soc. Neurosci.* **32**, 4755–4761 (2012).
72. Sun, X. & Lin, Y. Npas4: Linking neuronal activity to memory. *Trends Neurosci.* **39**, 264–275 (2016).
73. Khajehnejad, M. et al. Dynamic Network Plasticity and Sample Efficiency in Biological Neural Cultures: A Comparative Study with Deep Reinforcement Learning. *Cyborg Bionic Syst.* **6**, 0336 (2025).
74. Buzsáki, G. Two-stage model of memory trace formation: a role for 'noisy' brain states. *Neuroscience* **31**, 551–570 (1989).
75. Fuchsberger, T. & Paulsen, O. Modulation of hippocampal plasticity in learning and memory. *Curr. Opin. Neurobiol.* **75**, 102558 (2022).
76. Kennedy, M. B. Synaptic signaling in learning and memory. *Cold Spring Harb. Perspect. Biol.* **8**, a016824 (2016).
77. Kim, J. et al. Human assembloid model of the ascending neural sensory pathway. *Nature* <https://doi.org/10.1038/s41586-025-08808-3> (2025).
78. Kagan, B. J. et al. Harnessing Intelligence from Brain Cells In Vitro. *Neuroscientist*. 10738584251321438 <https://doi.org/10.1177/10738584251321438> (2025).
79. Morales Pantoja, I. E. et al. First Organoid Intelligence (OI) workshop to form an OI community. *Front. Artif. Intell.* **6**, 1116870 (2023).
80. Hartung, T. et al. The Baltimore declaration toward the exploration of organoid intelligence. *Front. Sci.* **1**, 1116870 (2023).
81. Tanveer, M. S. et al. Starting a synthetic biological intelligence lab from scratch. *PATTER* **6**, 101232 (2025).
82. Patel, H. et al. nf-core/mnaseq: nf-core/mnaseq v3.14.0 - Hassium Honey Badger. Zenodo <https://doi.org/10.5281/zenodo.10471647> (2024).
83. Di Tommaso, P. et al. Nextflow enables reproducible computational workflows. *Nat. Biotechnol.* **35**, 316–319 (2017).
84. Krueger, F. et al. FelixKrueger/TrimGalore: v0.6.10 - add default decompression path. Zenodo <https://doi.org/10.5281/zenodo.7598955> (2023).
85. Dobin, A. et al. STAR: ultrafast universal RNA-seq aligner. *Bioinformatics* **29**, 15–21 (2013).
86. Patro, R., Duggal, G., Love, M. I., Irizarry, R. A. & Kingsford, C. Salmon: fast and bias-aware quantification of transcript expression using dual-phase inference. *Nat. Methods* **14**, 417–419 (2017).
87. Martin, F. J. et al. Ensembl 2023. *Nucleic Acids Res.* **51**, D933–D941 (2023).
88. Quinlan, A. R. & Hall, I. M. BEDTools: a flexible suite of utilities for comparing genomic features. *Bioinformatics* **26**, 841–842 (2010).
89. Picard Tools - By Broad Institute. <https://broadinstitute.github.io/picard/>.
90. Li, H. et al. The Sequence Alignment/Map format and SAMtools. *Bioinformatics* **25**, 2078–2079 (2009).
91. Wang, L., Wang, S. & Li, W. RSeQC: quality control of RNA-seq experiments. *Bioinformatics* **28**, 2184–2185 (2012).
92. García-Alcalde, F. et al. Qualimap: evaluating next-generation sequencing alignment data. *Bioinformatics* **28**, 2678–2679 (2012).
93. Sayols, S., Scherzinger, D. & Klein, H. dupRadar: a Bioconductor package for the assessment of PCR artifacts in RNA-Seq data. *BMC Bioinforma.* **17**, 428 (2016).
94. Preseq | The Smith Lab. <https://smithlabresearch.org/software/preseq/>.
95. Love, M. I., Huber, W. & Anders, S. Moderated estimation of fold change and dispersion for RNA-seq data with DESeq2. *Genome Biol.* **15**, 550 (2014).
96. Mangiola, S., Molania, R., Dong, R., Doyle, M. A. & Papenfuss, A. T. tidybulk: an R tidy framework for modular transcriptomic data analysis. *Genome Biol.* **22**, 42 (2021).
97. Shannon, C. E. A mathematical theory of communication. *Bell Syst. Tech. J.* **27**, 379–423 (1948).
98. Pachitariu, M., Sridhar, S., Pennington, J. & Stringer, C. Spike sorting with Kilosort4. *Nat. Methods* **21**, 914–921 (2024).
99. Buccino, A. P. et al. SpikelInterface, a unified framework for spike sorting. *eLife* **9**, e61834 (2020).

Acknowledgements

We thank Dr. Paul Worley (Department of Neuroscience, Johns Hopkins University) for helpful discussions and antibody reagents. We thank George McNamara, PhD, the Ross Fluorescence Imaging Center (Johns Hopkins University), and the NIH shared instrumentation grant 1S10OD025244-01 for the use of the FV3000RS. We thank all members of the Center for Alternatives to Animal Testing for technical help and support. We gratefully acknowledge research support from the JHU SURPASS program. DA was supported by the National Institutes of Health (T32 ES007141) and International Foundation for Ethical Research Graduate Fellowship. M.S. was supported by the Deutsche Forschungsgemeinschaft (DFG, 507269789).

Author contributions

LS: Conceptualization, Methodology, Resources, Writing - Review & Editing, Supervision, Project Administration, and Funding acquisition. DA: Conceptualization, Methodology, Software, Validation, Formal analysis, Investigation, Writing - Original Draft. LM: Investigation and Validation. MS: Investigation and Writing - Review & Editing. JS, JL, AL, FH, TM, AM: Software, Formal Analysis, Visualization, and Writing - Review & Editing. EJ, TH, BK: Supervision, and Writing - Review & Editing. BK: Conceptualization. All authors contributed to the article and approved the submitted version.

Competing interests

T.H. is named inventor on a patent by Johns Hopkins University on the production of organoids, which is licensed to Axo-Sim, New Orleans, LA, USA. T.H. and L.S. are consultants for AxoSim, New Orleans, and T.H. is also a consultant for AstraZeneca and American Type Culture Collection (ATCC) on advanced cell culture methods. B.J.K. is a named inventor on patents by CCLabs Pty Ltd trading as Cortical Labs on the use of biological neural systems for intelligent purposes. B.J.K., F.H, and A.L are employees of Cortical Labs. B.J.K. and A.L. are shareholders of Cortical Labs. J.L is a data science consultant for Vindhya Data Science specializing in bioinformatics analysis. The rest of the authors declare no conflict of interest.

Additional information

Supplementary information The online version contains supplementary material available at <https://doi.org/10.1038/s42003-025-08632-5>.

Correspondence and requests for materials should be addressed to Lena Smirnova.

Peer review information *Communications Biology* thanks Wolfram Zimmermann and the other, anonymous, reviewer(s) for their contribution to the peer review of this work. Primary Handling Editor: Benjamin Bessieres. A peer review file is available.

Reprints and permissions information is available at <http://www.nature.com/reprints>

Publisher's note Springer Nature remains neutral with regard to jurisdictional claims in published maps and institutional affiliations.

Open Access This article is licensed under a Creative Commons Attribution-NonCommercial-NoDerivatives 4.0 International License, which permits any non-commercial use, sharing, distribution and reproduction in any medium or format, as long as you give appropriate credit to the original author(s) and the source, provide a link to the Creative Commons licence, and indicate if you modified the licensed material. You do not have permission under this licence to share adapted material derived from this article or parts of it. The images or other third party material in this article are included in the article's Creative Commons licence, unless indicated otherwise in a credit line to the material. If material is not included in the article's Creative Commons licence and your intended use is not permitted by statutory regulation or exceeds the permitted use, you will need to obtain permission directly from the copyright holder. To view a copy of this licence, visit <http://creativecommons.org/licenses/by-nc-nd/4.0/>.

© The Author(s) 2025